JOURNAL OF PETROLOGY | VOLUME 47 | NUMBER 1 | PAGES 3–33 | 2006 | doi:10.1093/petrology/egi062

The Role of Advective Fluid Flow and Diffusion during Localized, Solid-State Dehydration: Söndrum Stenhuggeriet, Halmstad, SW Sweden

DANIEL E. HARLOV[1]*, LEIF JOHANSSON[2], ALFONS VAN DEN KERKHOF[3] AND HANS-JÜRGEN FÖRSTER[1,4]

[1]GEOFORSCHUNGSZENTRUM POTSDAM, TELEGRAFENBERG, D-14473 POTSDAM, GERMANY

[2]DEPARTMENT OF GEOLOGY, UNIVERSITY OF LUND, SÖLVEGATAN 12, S-22362 LUND, SWEDEN

[3]GEOWISSENSCHAFTLICHES ZENTRUM DER UNIVERSITÄT GÖTTINGEN, GOLDSCHMIDTSTR. 3, D-37077 GÖTTINGEN, GERMANY

[4]INSTITUT FÜR GEOWISSENSCHAFTEN, UNIVERSITÄT POTSDAM, D-14415 POTSDAM, GERMANY

RECEIVED AUGUST 5, 2004; ACCEPTED JUNE 15, 2005
ADVANCE ACCESS PUBLICATION SEPTEMBER 5, 2005

A localized dehydration zone, Söndrum stone quarry, Halmstad, SW Sweden, consists of a central, 1 m wide granitic pegmatoid dyke, on either side of which extends a 2·5–3 m wide dehydration zone (650–700°C; 800 MPa; orthopyroxene–clinopyroxene–biotite–amphibole–garnet) overprinting a local migmatized granitic gneiss (amphibole–biotite–garnet). Whole-rock chemistry indicates that dehydration of the granitic gneiss was predominantly isochemical. Exceptions include [Y + heavy rare earth elements (HREE)], Ba, Sr, and F, which are markedly depleted throughout the dehydration zone. Systematic trends in the silicate and fluorapatite mineral chemistry across the dehydration zone include depletion in Fe, (Y + HREE), Na, K, F, and Cl, and enrichment in Mg, Mn, Ca, and Ti. Fluid inclusion chemistry is similar in all three zones and indicates the presence of a fluid containing CO_2, NaCl, and H_2O components. Water activities in the dehydration zone average 0·36, or $X_{H_2O} = 0{\cdot}25$. All lines of evidence suggest that the formation of the dehydration zone was due to advective transport of a CO_2-rich fluid with a minor NaCl brine component originating from a tectonic fracture. Fluid infiltration resulted in the localized partial breakdown of biotite and amphiboles to pyroxenes releasing Ti and Ca, which were partitioned into the remaining biotite and amphibole, as well as uniform depletion in (Y + HREE), Ba, Sr, Cl, and F. At some later stage, H_2O-rich fluids (H_2O activity $>0{\cdot}8$) gave rise to localized partial melting and the probable injection of a granitic melt into the tectonic fracture, which resulted in the biotite and amphibole recording a diffusion profile for F across the dehydration zone into the granitic gneiss as well as a diffusion profile in Fe, Mn, and Mg for all Fe–Mg silicate minerals within 100 cm of the pegmatoid dyke.

KEY WORDS: *charnockite; fluids; CO_2; brines; localized dehydration; Söndrum*

INTRODUCTION

Solid-state, high-grade dehydration of hornblende- and biotite-bearing rock, by low H_2O-activity fluids, to orthopyroxene ± clinopyroxene-bearing rocks on a localized scale (centimetres to metres) is a widespread phenomenon. The two principal dehydration reactions are

$$\underset{\text{hornblende}}{KCa_2(Fe,Mg)_4Al_3Si_6O_{22}(OH)_2} + \underset{\text{quartz}}{4\ SiO_2} = \underset{\text{clinopyroxene}}{Ca(Fe,Mg)Si_2O_6} + \underset{\text{orthopyroxene}}{3\ (Fe,Mg)SiO_3} + \underset{\text{plagioclase}}{CaAl_2Si_2O_8} + \underset{\text{K-feldspar}}{KAlSi_3O_8} + H_2O \quad (1)$$

*Corresponding author. E-mail: dharlov@gfz-potsdam.de

and

$$\underset{\text{biotite}}{K(Fe,Mg)_3AlSi_3O_{10}(OH)_2} + 3\,\underset{\text{quartz}}{SiO_2} = 3\,\underset{\text{orthopyroxene}}{(Fe,Mg)SiO_3} + \underset{\text{K-feldspar}}{KAlSi_3O_8} + H_2O. \quad (2)$$

Also referred to, more generally, as 'incipient' or 'arrested charnockitization', localized, solid-state dehydration zones occur worldwide, most commonly in amphibolite-facies terranes (e.g. inner Bjørnesund, Tasiusarsuaq terrane, SW Greenland—McGregor & Friend, 1992; the Adirondacks, New York—McLelland *et al.*, 1988; Kaapvaal craton, South Africa—van Reenen *et al.*, 1988; Kurunegala, Sri Lanka—Burton & O'Nions, 1990; Harris *et al.*, 1993; Seward Peninsula, Alaska—Todd & Evans, 1994; Harlov & Förster, 2002*a*; the Bamble Sector, SE Norway—Knudsen & Lidwin, 1996; Nijland *et al.*, 1998; the Rogaland area, SW Norway—Vander Auwera, 1993; the Quetico subprovince, Ontario, Canada—Pan & Fleet, 1996). However, they also can occur in granitoids (e.g. Natal, South Africa—van den Kerkhof & Grantham, 1999). Localized dehydration zones were first described, and have subsequently been extensively documented, in the Archean amphibolite-facies terranes of southern India (e.g. Friend, 1981; Hansen *et al.*, 1984, 1987; Srikantappa *et al.*, 1985; Kumar & Chacko, 1986; Santosh, 1986, 1992, 2003; Stähle *et al.*, 1987; Harris & Bickle, 1989; Santosh *et al.*, 1990, 1991*a*, 1991*b*; Yoshida *et al.*, 1991; Jackson & Santosh, 1992; Harris *et al.*, 1993; Raith & Srikantappa, 1993; Santosh & Wada, 1993*a*, 1993*b*; Santosh & Radhika, 1994; Yoshida & Santosh, 1994; Harley & Santosh, 1995; Rajesh *et al.*, 1997; Satish-Kumar & Santosh, 1998; Dobmeier & Raith, 2000; Kumar, 2004). In some cases, depending on *PT* conditions and X_{H_2O}, localized, CO_2–brine-induced dehydration can be complicated by apparent partial melting (e.g. Burton & O'Nions, 1990; Perchuk *et al.*, 2000).

Sources for low H_2O activity fluids include magmatic dykes (e.g. Knudsen & Lidwin, 1996; van den Kerkhof & Grantham, 1999), volatile-rich rocks such as marbles (e.g. McLelland *et al.*, 1988; Harlov & Förster, 2002*a*), or tectonic features such as cracks and/or shear zones, which act as conduits for fluid flow from a distant source (e.g. Hansen *et al.*, 1987; Harris & Bickle, 1989; Radhika & Santosh, 1996). Fluid inclusion data indicate that CO_2, coupled with a minor NaCl–KCl-rich brine fraction, are the principal components in the dehydrating fluid (e.g. Andersen *et al.*, 1997; Tsunogae *et al.*, 2002; Fonarev *et al.*, 2003; Santosh & Tsunogae, 2003; Sarkar *et al.*, 2003). Experimentally, fluids consisting only of NaCl and KCl brines are known to have relatively low wetting angles (see Watson & Brenan, 1987; Gibert *et al.*, 1998). This potentially would allow them to flow along grain boundaries over relatively large distances (e.g. on the kilometre scale; Newton *et al.*, 1998). In contrast, CO_2-rich fluids along the CO_2–H_2O join (500–1300 MPa; 950–1200°C) are known to have large wetting angles such that they do not form an interconnected network along grain boundaries, but rather isolated pockets of fluid, primarily at three-grain junctions (Watson & Brenan, 1987; Brenan & Watson, 1988; Holness, 1997; Gibert *et al.*, 1998). The inability of CO_2 to flow easily along grain boundaries limits its ability to penetrate deep into the rock, resulting in dehydration zones extending from centimetres to metres only. This observation is supported by $\delta^{18}O$ isotope studies of incipient charnockite formation in southern India, which suggest that high-grade, CO_2-rich fluids have a limited infiltration range of *c.* 2 m under granulite-grade conditions (Harris & Bickle, 1989). However, there are cases of CO_2-induced dehydration zones extending as much as 10 m (e.g. van den Kerkhof & Grantham, 1999).

In this study, a comprehensive investigation is made on samples collected along a 1260 cm traverse consisting of a central pegmatoid dyke surrounded by a localized dehydration zone in a migmatized granitic gneiss, all of which are exposed along one of the walls of the Söndrum stone quarry, Halmstad, SW Sweden. The obvious structural and geometric relationship between these three rock types makes this association ideally suited for the study of fluid-induced dehydration in high-grade rocks. Whole-rock and trace element chemistry is investigated, coupled with a detailed documentation of the petrographic fabric, mineralogy, and mineral chemistry of each sample. In addition, a detailed study is made of the fluid inclusions in specific samples along the traverse. Systematic changes in the mineral chemistry, whole-rock chemistry, and fluid inclusion data, both in the dehydration zone and the granitic gneiss, relative to the central pegmatoid dyke, are used to identify the nature of the dehydrating fluids during advective fluid flow with regard to element depletion and enrichment. These profiles are also used to discern the role of later fluids in the diffusion of specific elements.

GEOLOGICAL SETTING

Regional geology

Rocks in the SW Swedish granulite region (SGR) consist predominantly of granitic to tonalitic orthogneisses (*c.* 1660–1700 Ma), with minor intermediate to mafic units (Fig. 1) (Larson *et al.*, 1990; Johansson *et al.*, 1993; Connelly *et al.*, 1996; Söderlund *et al.*, 1999, 2002). The SGR extends along the Kattegatt coast from Hallandsås to the Varberg–Torpa charnockite–granite complex (Fig. 1b). In general, orthopyroxene–clinopyroxene-bearing granitic bodies in the Swedish portion of the Baltic Shield tend to crop out primarily in the SGR.

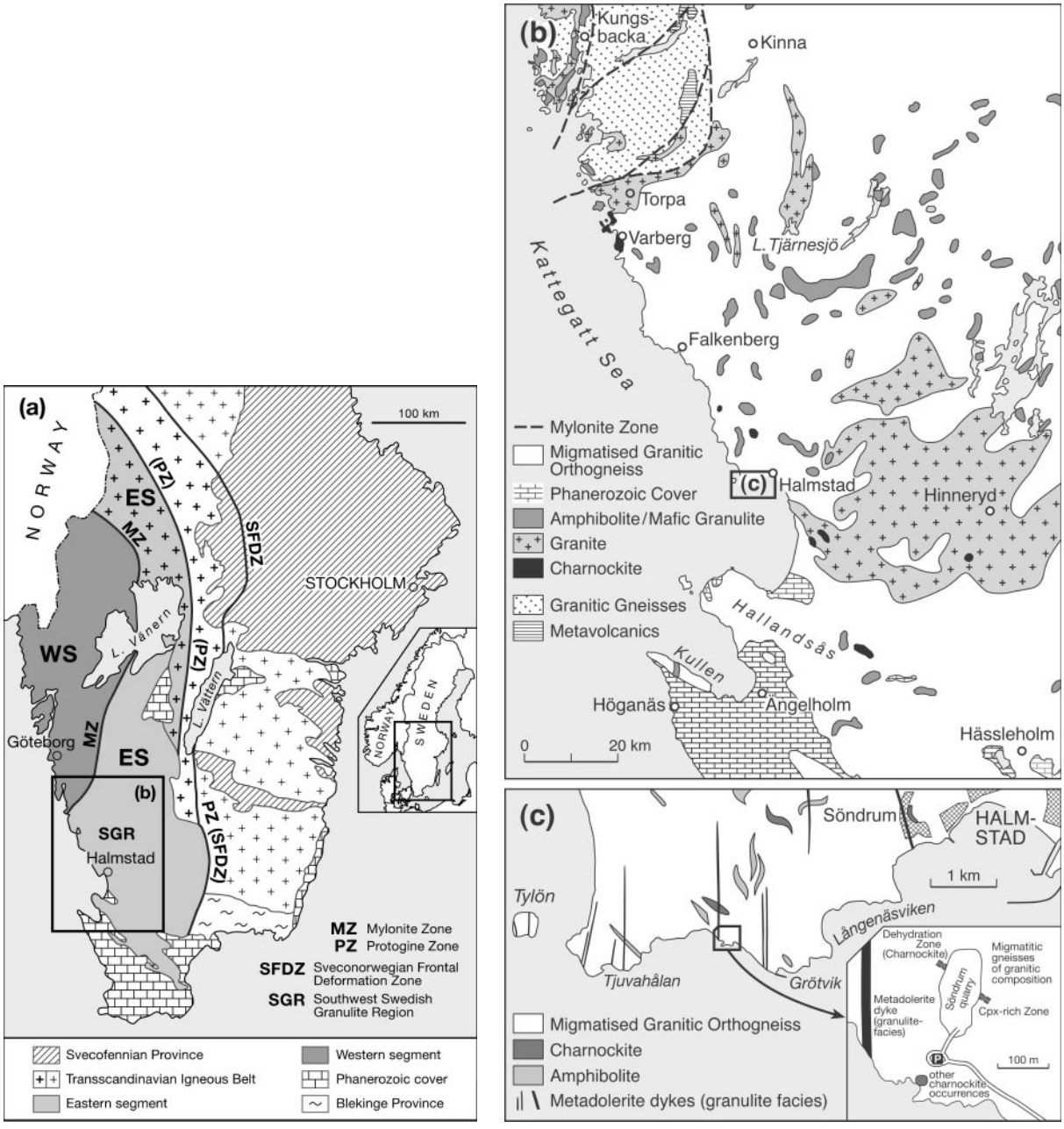

Fig. 1. (a) General geological map of southern Sweden showing the location of the so-called Eastern Segment (ES), Western Segment (WS), and the location of the SW Swedish granulite region (SGR). The Eastern Segment is bounded by two major, steep zones of Sveconorwegian shear deformation known as the Mylonite Zone and the Protogine Zone. (b) The general geology of the SGR. The SGR extends along the Kattegatt coast from Hallandsås to the Varberg–Torpa charnockite–granite complex. In the Swedish portion of the Baltic Shield, orthopyroxene–clinopyroxene-bearing granitic bodies (here loosely termed charnockites) crop out primarily in the SGR. Of these bodies, the Varberg–Torpa charnockite–granite complex is the largest known. (c) The local geology in the immediate area of Halmstad including the location of the Söndrum stone quarry. The inset shows a sketch of the quarry indicating the location of the pegmatoid dyke and the surrounding orthopyroxene–clinopyroxene-bearing dehydration zone. Also shown is the location of the clinopyroxene-rich dehydration zone as described in the text. Geology along the Kattegatt coast, the Söndrum area, and the SGR in general is taken from Larsson (1956) and from compilations by the Geological Survey of Sweden.

Of these, the Varberg–Torpa charnockite–granite complex is the principal one. Although the location of some of the larger charnockite bodies is noted in Fig. 1b, a complete, systematic mapping of all known occurrences of orthopyroxene–clinopyroxene-bearing granitic bodies in the SGR has, so far, never been done.

Rocks in the SGR were affected by a major metamorphic event, *c.* 1420–1460 Ma (Söderlund *et al.*, 1999),

during which migmatization and penetrative deformation of the granitic gneiss occurred throughout the region. At least two generations of granites, quartz monzonites, and syenites (*c.* 1400 Ma and 1200 Ma) have intruded the SGR. These include the Varberg–Torpa charnockite–granite complex and the Tjärnesjö granite at 1400–1370 Ma (Andersson *et al.*, 1999). The last major tectonothermal event that affected the SGR was the Sveconorwegian orogeny at *c.* 950–970 Ma (Johansson *et al.*, 2001). This event was characterized by metamorphic conditions that ranged from upper amphibolite to granulite grade (680–750°C and 850–1170 MPa) (Wang & Lindh, 1996), which in some places grades into eclogite-facies metamorphism (Möller, 1998). Subsequent cooling of the SGR during exhumation is compatible with 925–945 Ma U–Pb titanite (Connelly *et al.*, 1996; Wang *et al.*, 1996) and Ar–Ar hornblende geochronology indicating blocking temperatures of 500°C by 930 Ma (Page *et al.*, 1996).

The Söndrum stone quarry

In a local stone quarry in the Söndrum area, two elongated, 'fracture-controlled' dehydration zones in the local migmatitic granitic gneiss are well exposed along two opposing walls (Fig. 1c). At present, they represent the only known examples of localized dehydration in the region surrounding Halmstad. The two zones differ distinctly with respect to lithology, mineralogy, and structure. The one along the eastern wall consists of a 0·5 m wide, dark green, orthopyroxene-absent zone rich in clinopyroxene and surrounded on either side by a 0·5 m wide, diffuse orthopyroxene- and clinopyroxene-bearing brown–green overprint of the host, red–pink granitic gneiss. The second zone, which is the focus of this study, occurs opposite on the western wall. It takes the form of a metre-wide pegmatoid dyke of granitic composition from which, on either side, extends an approximately 2·5–3 m wide margin consisting of an orthopyroxene- and clinopyroxene-bearing, brown–green dehydration zone. Significantly, this dehydration zone again overprints the migmatization and banding of the granitic gneiss (Fig. 2a and b).

The pegmatoid dyke consists primarily of coarse K-feldspar, plagioclase, and quartz crystals as well as graphic intergrowths of feldspar and quartz (Fig. 2c). Clinopyroxene laths, up to 3 cm long, often with a thin black margin of amphibole, are present along with large amphibole crystals, also up to 3 cm long. In other parts of the pegmatoid dyke, the K-feldspar megacrysts have been recrystallized into a granular, relatively fine-grained mass of microcline.

Both the dehydration zone and the surrounding granitic gneiss have identical migmatized gneissic textures and, with the exception of orthopyroxene, clinopyroxene, biotite, and amphibole, have identical modal mineralogies (quartz–plagioclase–K-feldspar–garnet–magnetite–ilmenite–pyrrhotite–pyrite–chalcopyrite–graphite–fluorapatite–allanite–zircon). Gneissic banding is defined by the Fe–Mg silicate minerals. The one difference is that, in the dehydration zone, specific grains of hornblende and biotite are completely replaced by orthopyroxene and clinopyroxene. However, both the orthopyroxene and clinopyroxene show some sporadic, partial rehydration in the form of a scattering of relatively small biotite and amphibole crystals along the pyroxene grain rim. Large grains of allanite, surrounded by a spider's web of radiating cracks (Fig. 2d), typically visible to the naked eye, are present both in the dehydration zone as well as in the surrounding granitic gneiss. The contact between the pegmatoid dyke and the dehydration zone is relatively sharp, in contrast to the contact between the dehydration zone and the amphibolite-facies gneiss, which is more patchy over *c.* 20 cm.

Zircon, from the dehydration zone and granitic gneiss, exhibits a pronounced oscillatory growth zoning, with U-poor cores and a series of U-rich rims. Both the core and inner rim of these zircons yield an ion microprobe age of *c.* 1670 Ma, which dates the regional crystallization of the granitic precursor that was migmatized to a granitic gneiss during regional metamorphism at *c.* 1420–1460 Ma (Söderlund *et al.*, 2002). Ion-probe dating of unzoned zircons from the pegmatoid dyke yields an age of *c.* 1400 Ma, which dates the formation of the pegmatoid dyke. Zircons from the dehydration zone have an additional thick rim, which has also been dated at *c.* 1400 Ma, thus confirming that the formation of the pegmatoid dyke and dehydration zone were concurrent (Johansson, 1998; Rimsa *et al.*, 2003). Very thin, outer rims on the zircons, from both the dehydration zone and granitic gneiss, were formed during the *c.* 970 Ma Sveconorwegian orogeny.

ANALYTICAL TECHNIQUES

Sample selection

The goal of this project was to undertake a systematic study of petrographic relationships and mineral chemistry across apparent metamorphic grade on a localized scale. This required selecting samples of the gneiss at a minimum of 15 cm intervals (and multiples thereof) along a traverse outwards from the approximate centre of the pegmatoid dyke across the dehydration zone deep into the granitic gneiss (see Fig. 2b). A total of 34 samples were studied. These included three from the pegmatoid dyke (first 0–40 cm), 19 from the dehydration zone (next 40–320 cm), and 12 from the granitic gneiss (last 320–1260 cm). The distance (in centimetres) of a particular sample from the approximate centre of the pegmatoid dyke is noted in the sample designation by the last number.

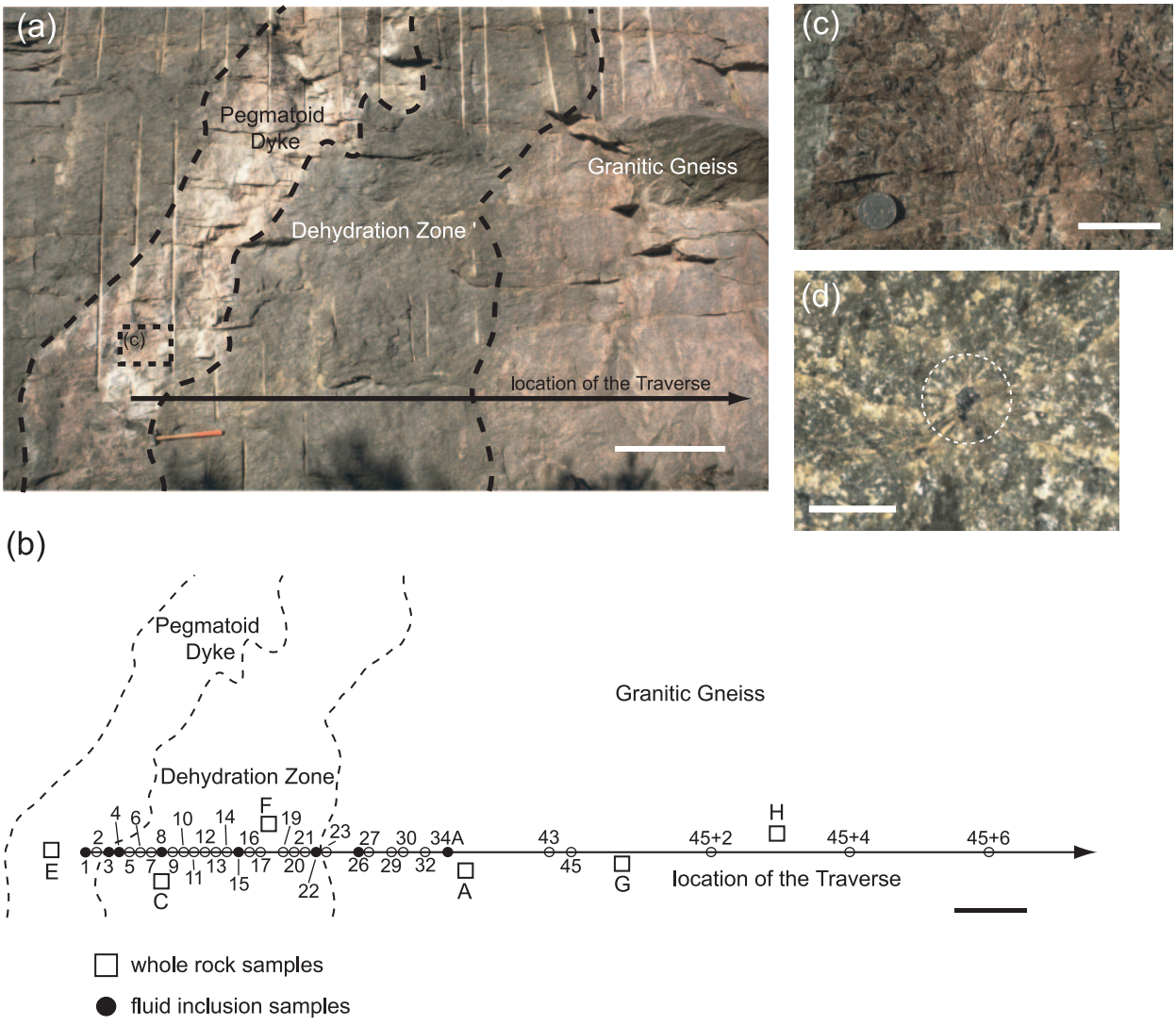

Fig. 2. (a) Photograph showing the pegmatoid dyke and surrounding dehydration zone, along with the approximate location of the sample traverse. (b) Schematic diagram showing the approximate location of the pegmatoid dyke and the dehydration zone relative to sample locations along the entire traverse. Locations, where samples were taken for whole-rock analysis, are designated by boxes and the letter in the sample label (e.g. E = HD26E). To avoid overcrowding, samples are designated by the middle number in the label (e.g. SD8105 is 8, SD9120 is 9, etc.). (c) Close-up of the pegmatoid dyke. The graphic intergrowth of feldspar and quartz should be noted. (d) Close-up of one of the large allanite grains in the dehydrated migmatized gneiss. The radiating cracks surrounding the allanite grain should be noted. Scale bar in (a) and (b) represents 1 m. Scale bar in (c) represents 2 cm. Scale bar in (d) represents 1 cm.

Whole-rock analysis

The samples were analysed at CNRS-CRPG, Service d'Analyse des Roches et des Minéraux (SARM) in Nancy, France. The analytical procedure has been described in detail by Carignan *et al.* (2001). Rock samples (3–4 kg) from each of the locations shown in Fig. 2b were powdered and fused in Pt crucibles along with $LiBO_2$ at 980°C in an automatic tunnel oven. Major and trace elements were measured using, respectively, inductively coupled plasma atomic emission spectrometry (ICP-AES) and flow injection inductively coupled plasma mass spectrometry (ICP-MS). A blank and five international geostandards were used (Govindaraju, 1994). Analysis for fluorine was performed using ion-selective electrodes. Total H_2O and CO_2 were determined by combustion IR detection (Förster *et al.*, 1999). Whole-rock analyses of the pegmatoid, dehydration zone, and granitic gneiss are presented in Table A1, contained in Electronic Appendix 1, which may be downloaded from the *Journal of Petrology* website at http://www.petrology.oupjournals.org.

LA-ICP-MS (laser ablation–inductively coupled plasma mass spectrometry)

The REE abundances in garnet were determined at the Department of Geology, Gothenburg University, Sweden, using a CETAC LSX200 laser ablation sampler attached to a Hewlett Packard 4500 quadrupole ICP-MS system. Analytical procedures have been described by Bi *et al.* (2001). A 25 μm diameter UV laser was operated in 4 Hz pulsed mode for about 90 s on each spot, with 30 s of background counting, before activation of the laser. The time-resolved spectra were inspected, spikes caused by surface contamination or inclusions were avoided, and three time intervals were chosen for each spot to evaluate precision. ^{30}Si was used as the internal standard and the NIST 612 glass as the concentration standard for the REE.

PIXE (proton-induced X-ray emission)

Nuclear microprobe analyses were undertaken at the Lund nuclear microprobe, which is linked to a 3 MeV single-ended accelerator (Johansson & Campbell, 1988). Analyses were carried out with either 2·55 or 2·82 MeV protons. For detection of X-rays a 50 mm^2, Si(Li) detector with a resolution of less than 155 eV was employed. The detector was equipped with a Mylar filter of either 425 or 775 μm thickness to suppress intense low-energy X-ray lines from major elements.

Electron microprobe (EMP) analysis

Electron microprobe (EMP) analyses of plagioclase and K-feldspar (Table A2a and b), biotite (Table A3), amphibole (Table A4), garnet (Table A5), clinopyroxene (Table A6), orthopyroxene (Table A7), ilmenite (Table A8), fluorapatite (Table A9), and allanite (Tables A10a and b) were carried out using the CAMECA SX50 and SX100 electron microprobes at the GeoForschungsZentrum Potsdam. (Tables A1–A10 are contained in Electronic Appendix 1 and may be downloaded from the *Journal of Petrology* website at http://www.petrology.oupjournals.org.) Unless otherwise specified, only mineral cores were analysed and mineral rims were avoided. This was done to obtain mineral compositions that are as close as possible to the peak metamorphic conditions present during formation of the dehydration zone. This assumes that these mineral cores were in equilibrium during the dehydration event. Mineral rims, which normally record post-peak metamorphic processes present during uplift and cooling, were avoided.

Analytical conditions for the silicates and oxides consisted of a 15 kV acceleration voltage, 20 nA beam current, and counting times of 10–30 s depending on the element. Beam spot size was 1 μm for garnet and the pyroxenes, 5 μm for biotite and amphibole, and 15 μm for feldspar, ilmenite, apatite, and allanite. Silicate and oxide standards were taken from both the CAMECA and Smithsonian standard sets (Jarosewich *et al.*, 1980). The CAMECA PAP program was used for matrix correction (Pouchou & Pichoir, 1985). Reintegration of K-feldspar grains with exsolution lamellae of albite involved a systematic succession of 15 μm diameter electron beam spot analyses in a crosswise sweep such that the entire surface of the mineral grain was sampled. Individual analyses (up to 278 per grain) were then averaged to produce a composite analysis (Tables A2a and b). From two to 12 silicate and oxide grains, scattered evenly over the length and breadth of the thin section, were analysed per sample. To ensure that the relative differences observed are correct within microprobe error (+/-1 oxide wt %), silicate and oxide analyses per sample were obtained during one single measuring session including multiple checks of the calibration. The full EMP dataset, representing all individual silicate and oxide analyses, is contained in Electronic Appendix 2 and may be downloaded from the *Journal of Petrology* website at http://www.petrology.oupjournals.org.

Elements analysed for fluorapatite and allanite included P, Si, Y, La, Ce, Nd, Sm, Gd, Dy, Yb, Ca, Mn, Fe, Sr, Ba, Na, F, and Cl, with counting times of 20–120 s depending on the relative amount of the element. Technique and counting times for the [Y + rare earth elements (REE)] have been described by Harlov & Förster. (2002*b*). Standards for the REE were taken from synthetic REE phosphates prepared by Jarosewich & Boatner (1991), with the remaining standards taken from the Durango fluorapatite and the Smithsonian oxide and silicate standard set (Jarosewich *et al.*, 1980). From five to 15 fluorapatite or allanite grains were analysed per sample in a relatively even sampling over the entire breadth and length of the thin section. If possible, both the core and rim were sampled. No systematic difference was seen. The full EMP dataset, representing all individual fluorapatite and allanite analyses, is contained in Electronic Appendix 3 and may be downloaded from the *Journal of Petrology* website at http://www.petrology.oupjournals.org.

Microthermometry

Phase transitions in fluid inclusions were investigated by using a Linkam THMS 600 heating–freezing stage cooled with liquid nitrogen (Shepherd, 1981). Samples were prepared as unmounted, doubly polished sections, with an average thickness of 0·2 mm. The stage was calibrated using a set of synthetic fluid inclusion standards. For temperatures around −56·6°C (the melting point of CO_2) and around 0°C, the accuracy is better than 0·5°C, whereas for temperatures between 200 and 600°C, the accuracy is better than 5°C.

WHOLE-ROCK CHEMISTRY

The amphibolite-facies granitic gneiss and dehydrated granitic gneiss show nearly identical major element

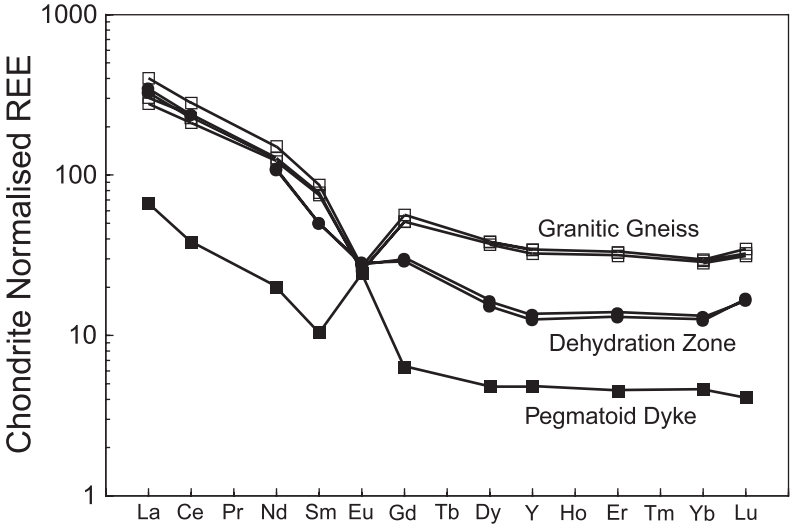

Fig. 3. Whole-rock, chondrite-normalized (Y + REE) distribution patterns for the pegmatoid dyke, the dehydration zone, and the original granitic gneiss. Chondrite values are taken from Anders & Grevesse (1989).

compositions. Compared with the granitic gneiss, the dehydration zone is enriched in Ba and Sr and depleted in F (Table A1). Differences in (Y + REE) between the dehydration zone and the granitic gneiss are more pronounced (Fig. 3). Whereas the light REE (LREE) contents, up to Nd, show similar abundances, the heavy REE (HREE; including Y and Sm) are markedly depleted in the dehydration zone. In general, the pegmatoid dyke has a similar, but slightly more evolved major element composition than either the dehydration zone or the granitic gneiss. However, it is higher in Rb and Sr and lower in (Y + REE), Sc, and F relative to both the dehydration zone and the granitic gneiss. The one exception is Eu, whose abundance remains unchanged across the entire traverse. The positive Eu anomaly of the feldspar-rich pegmatoid dyke indicates that the oxidation state of Eu must have been 2+ as opposed to 3+, thus allowing it to be strongly partitioned into the plagioclase where it substitutes for Ca. Water and CO_2 do not show much variance across the traverse although there is some indication that CO_2 might be slightly depleted in the dehydration zone compared with the granitic gneiss.

MINERAL TEXTURES AND CHEMISTRY

Across the traverse, starting at the centre of the pegmatoid dyke, certain trends in mineral populations and mineral chemistry are seen. All minerals, with the exception of orthopyroxene, clinopyroxene, and magnetite, are ubiquitous, showing the same modal mineralogy both in the dehydration zone as well as in the surrounding granitic gneiss, with the proviso that in the case of those samples containing orthopyroxene and clinopyroxene, modal amounts of hornblende and biotite are relatively less than in samples devoid of pyroxenes.

Feldspars

Feldspar–quartz textures and chemistry in the dehydration zone are identical to those in the surrounding granitic gneiss (Fig. 4a–d). Plagioclase (Table A2a) is enriched in albite ($X_{Ab} \approx 0{\cdot}83$–$0{\cdot}84$). This albitic component is reflected in the K-feldspar ($X_{Kfs} \approx 0{\cdot}2$–$0{\cdot}3$; Table A2b), which shows numerous exsolution lamellae of albite as well as diffusion of Na into the plagioclase along the grain boundary between K-feldspar and plagioclase (Fig. 4b and d). In addition, myrmekite-like lamellae of quartz occur in the plagioclase (Fig. 4e) as well as, more rarely, anti-perthite (Fig. 4f). Plots of plagioclase and K-feldspar compositions from the same thin section on the feldspar ternary indicate disequilibrium between the two phases.

Biotite

Various trends in the biotite chemistry along the traverse are shown in Fig. 5 (see Table A3). In general, per sample, the composition of independent biotite grains is identical, within EMP error, with biotite grains associated with the pyroxenes. Of special note is the Ti content, which is relatively higher in biotite from the dehydration zone compared with biotite in the granitic gneiss (Fig. 5a). The Ti content suddenly drops at the boundary between the dehydration zone and the granitic gneiss. In contrast, biotite is depleted in Fe in the first 100–150 cm of the dehydration zone outwards from the pegmatoid dyke (Fig. 5b). Complementing this loss in Fe are the Mn (Fig. 5c) and Mg contents (not plotted), which show a

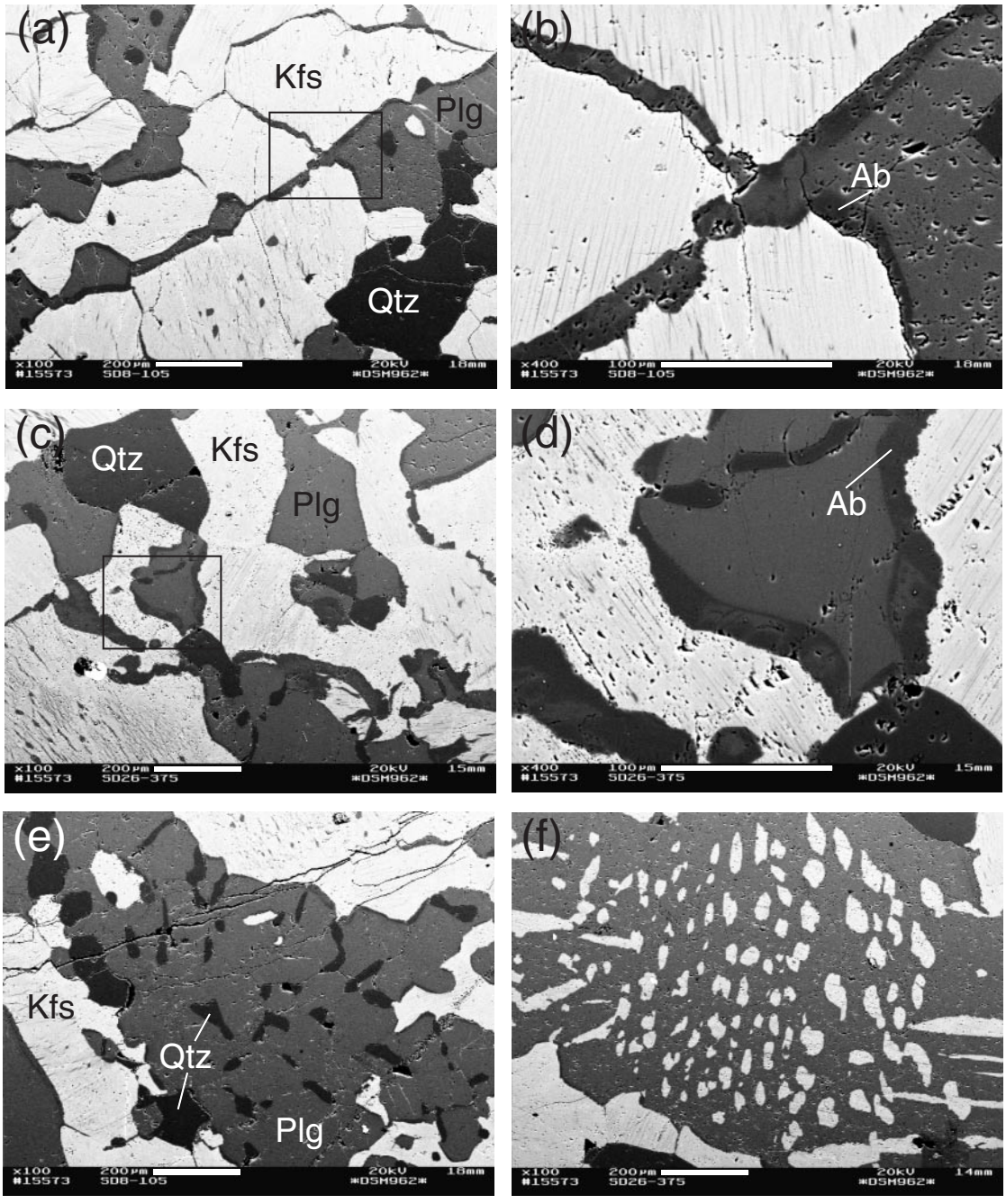

Fig. 4. BSE images showing a variety of typical K-feldspar–albite–plagioclase–quartz textures in both the dehydration zone (a, b, e) and the granitic gneiss (c, d, f). (b) is an enlargement of the area outlined by the black box in (a); (d) is an enlargement of the area outlined by the black box in (c).

sharp increase in the immediate vicinity of the pegmatoid dyke, followed by a gentle dip, and then a gradual increase moving outwards into the granitic gneiss.

The logarithms of the HF and HCl fugacities relative to H_2O, for a fluid in equilibrium with biotite, were estimated using the calibrations of Munoz (1992), which incorporate the updated experimental data of Zhu & Sverjensky (1991, 1992). Fluorine and Cl contents in biotite from the dehydration zone, especially in the vicinity of the pegmatoid dyke, display contrasting trends (Fig. 5d–f). Chlorine is uniformly depleted throughout the dehydration zone, whereas F abundances, although showing their greatest depletion at the contact with the pegmatoid dyke, display a gradual increase along the

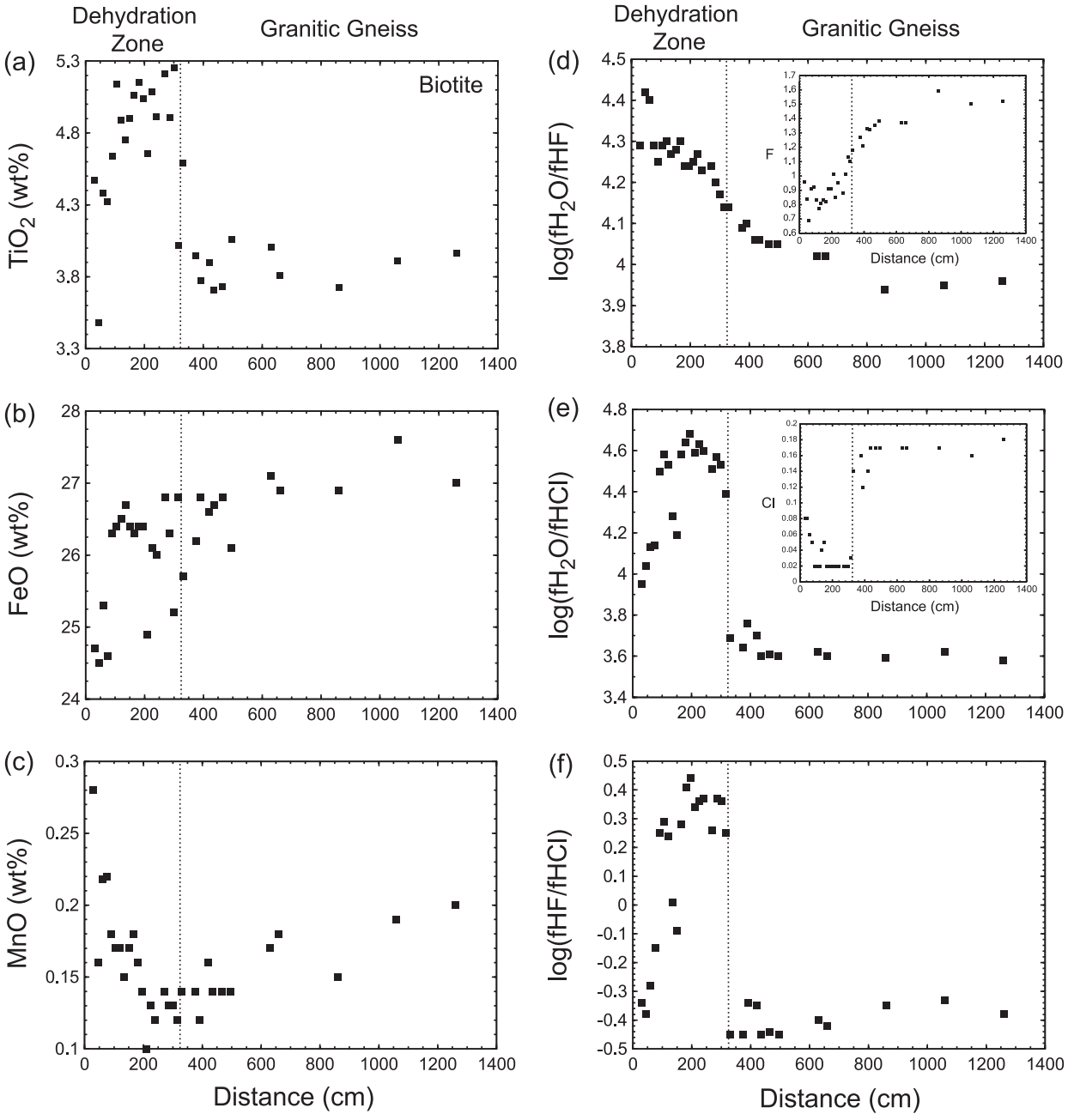

Fig. 5. Plot of biotite chemistry as a function of distance (cm) along the traverse outwards from the centre of the pegmatoid dyke (0 cm) for TiO_2 (a), FeO (b), MnO (c), f_{H_2O} relative to f_{HF} (d), f_{H_2O} relative to f_{HCl} (e), and f_{HF} relative to f_{HCl} (f). Dotted line designates the approximate boundary between the dehydration zone and the granitic gneiss. The first symbol in each plot designates the boundary with the pegmatoid dyke. The logarithms of HF and HCl fugacities relative to H_2O for a fluid in equilibrium with biotite were estimated using the calibrations of Munoz (1992), which incorporate the updated experimental data of Zhu & Sverjensky (1991, 1992). Also shown in (d) and (e) are insets of plots of F and Cl, respectively, vs distance (cm).

traverse, evening out at 800 cm with the apparent mean F content in biotite from the granitic gneiss.

Amphibole

EMP analysis of the amphiboles indicates that they belong to a group of sodic–calcic amphiboles termed taramite, ideally $Na(CaNa)Fe_3^{2+}AlFe^{3+}Si_6Al_2O_{22}(OH)_2$ according to IMA-approved nomenclature (Leake *et al.*, 1997). Amphibole analyses, given in Table A4, suggest that Ti probably substitutes for Al, whereas K and Na are positioned on the Ca site. Amphibole mineral chemistry along the traverse mirrors that of the biotite (Fig. 6).

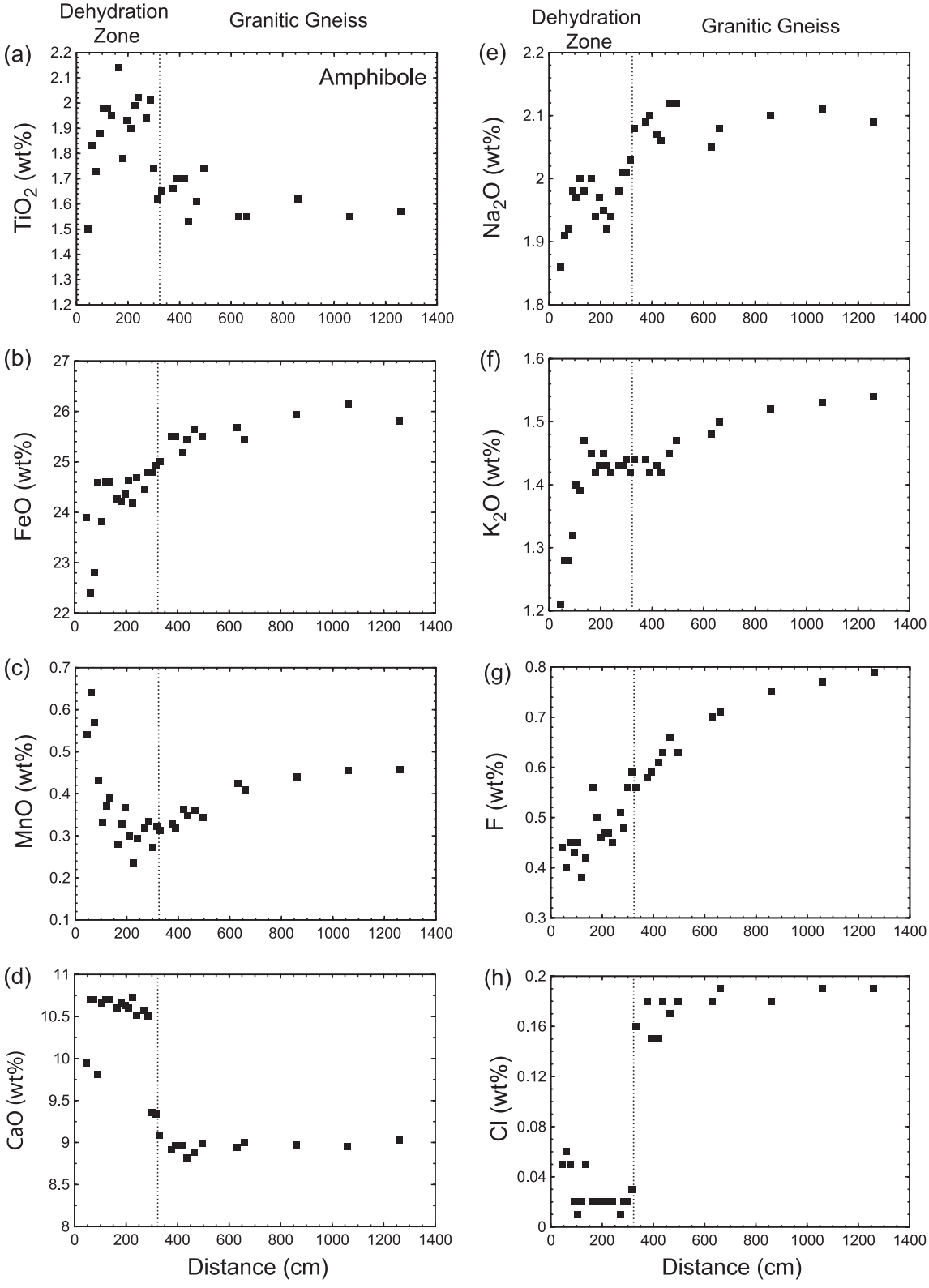

Fig. 6. Plot of amphibole chemistry as a function of distance (cm) along the traverse outwards from the centre of the pegmatoid dyke for TiO_2 (a), FeO (b), MnO (c), CaO (d), Na_2O (e), K_2O (f), F (g), and Cl (h). Dotted line designates the approximate boundary between the dehydration zone and the granitic gneiss. The first symbol in the plot designates the boundary with the pegmatoid dyke.

Here, amphibole in the dehydration zone has higher Ti and lower Fe contents than in the granitic gneiss (Fig. 6a and b). Manganese (Fig. 6c), as well as Mg (not plotted), shows a sharp increase in the immediate vicinity of the pegmatoid dyke, followed by a shallow dip, and then gradually increases to a constant value deep within the granitic gneiss. Whereas the Ca content in the amphibole is uniformly higher in the dehydration zone than in the granitic gneiss, both Na and K show a sharp depletion in amphibole in the immediate vicinity of the pegmatoid dyke, followed by an intermediate 'plateau' value throughout the rest of the dehydration zone, and a gradual increase in content moving along the traverse into the granitic gneiss (Fig. 6d–f). Both F and Cl chemistry mimic that observed in the biotite showing marked depletion in the dehydration zone (Fig. 6g and h). Moving into the granitic gneiss, F displays the same gradual increase seen in the biotite, although more pronounced, again evening out to what is presumably the mean F content in amphibole in the granitic gneiss. In contrast, Cl shows a sudden jump at the boundary with the granitic gneiss, whereas afterwards it approximates a constant value.

Garnet

Garnet occurs as relatively small (5–100 μm), anhedral grains with numerous vermicular inclusions of quartz and feldspar. They are commonly in association with the pyroxenes, biotite, and amphibole. There is no change in garnet textures across the dehydration zone into the granitic gneiss. Garnet chemistry across the traverse is relatively consistent, with the exception of Mn, Fe, and (Y + HREE) (Figs 7 and 8; Table A5). Manganese and Mg (not plotted) again show a sharp increase in the immediate vicinity of the pegmatoid dyke, whereas Fe mirrors this increase by showing a relatively sharp decrease. LA-ICP-MS and PIXE analysis of garnet indicate that garnet from the dehydration zone, and rare garnet in the pegmatoid dyke, is depleted in (Y + HREE) compared with garnet from the granitic gneiss (Fig. 8).

Pyroxenes

Pyroxenes occur only in the dehydration zone, in addition to rare clinopyroxene in the pegmatoid dyke. Going outwards from the boundary with the pegmatoid dyke, only clinopyroxene is found in the first 80–85 cm. Orthopyroxene appears at this point and is the predominant pyroxene for the next 85–290 cm, with clinopyroxene still present, though sporadically. A second clinopyroxene zone, in which orthopyroxene is again absent, starts at around 290–295 cm and continues to the patchy boundary with the granitic gneiss at about 320–325 cm. Both orthopyroxene and clinopyroxene

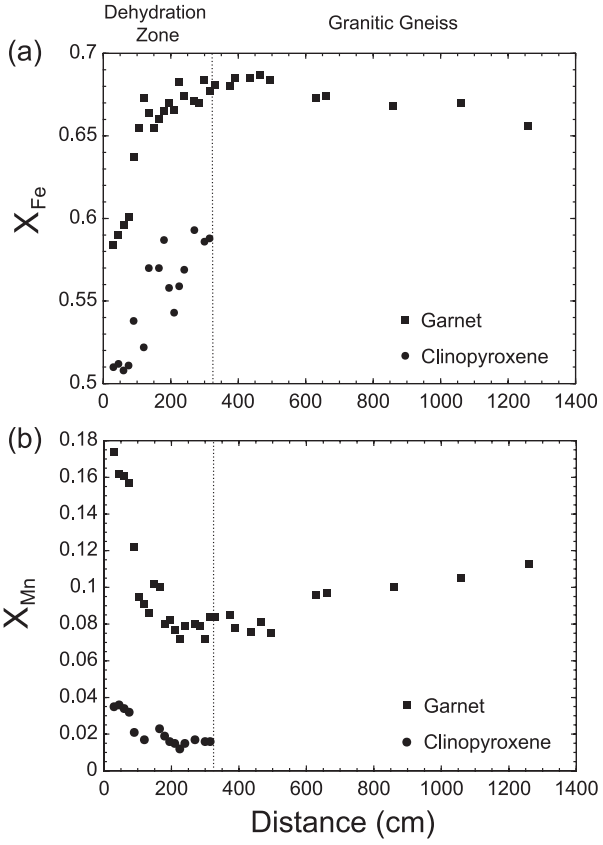

Fig. 7. Plot of garnet and clinopyroxene chemistry as a function of distance along the traverse outwards from the centre of the pegmatoid dyke for X_{Fe} = Fe/(Fe + Mg + Mn) (a) and X_{Mn} = Mn/(Fe + Mg + Mn) (b), both in a.p.f.u. Dotted line designates the approximate boundary between the dehydration zone and the granitic gneiss. The first symbol in the plot designates the boundary with the pegmatoid dyke.

show no specific relationship with the surrounding minerals, with the exception of random retrograde grains of biotite and amphibole scattered along the pyroxene grain rims.

Clinopyroxene chemistry mirrors that of the garnet, although less dramatically (Fig. 7; Table A6). Manganese and Mg (not plotted) show a moderate increase in the immediate vicinity of the pegmatoid dyke, whereas Fe shows a more dramatic decrease. Iron strongly increases across the width of the dehydration zone as a function of distance from the pegmatoid dyke.

Orthopyroxene chemistry is relatively constant across the width of the dehydration zone, with the exception of samples SD9-120, SD15-210, and SD17-240, which contain two orthopyroxene populations (Table A7). The two populations are distinguished by a difference of about 0·05 in X_{Fe}, with some indication that the population richer in Fe is also richer in Mn. Possible faint trends in Mn and Fe, similar to those seen in the clinopyroxene, are also observed in the orthopyroxene, but are within

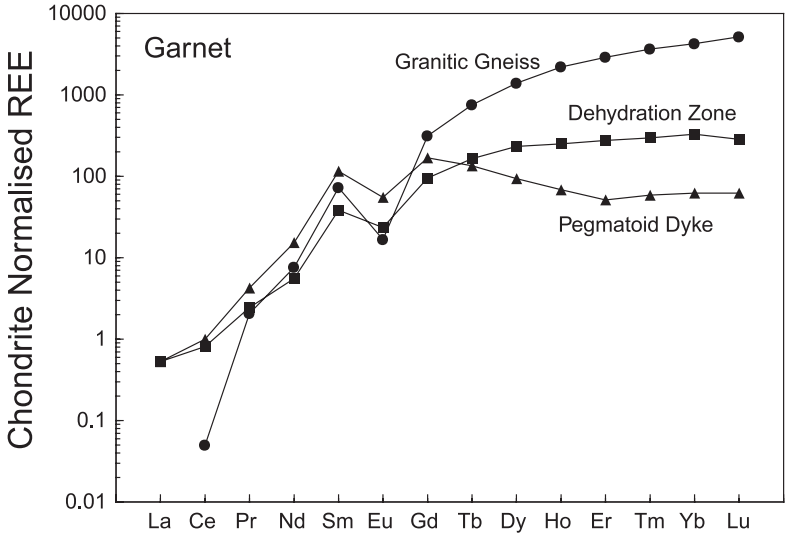

Fig. 8. Chondrite-normalized REE distribution pattern for garnet from the pegmatoid dyke, the dehydration zone, and the granitic gneiss. Chondrite values are taken from Anders & Grevesse (1989).

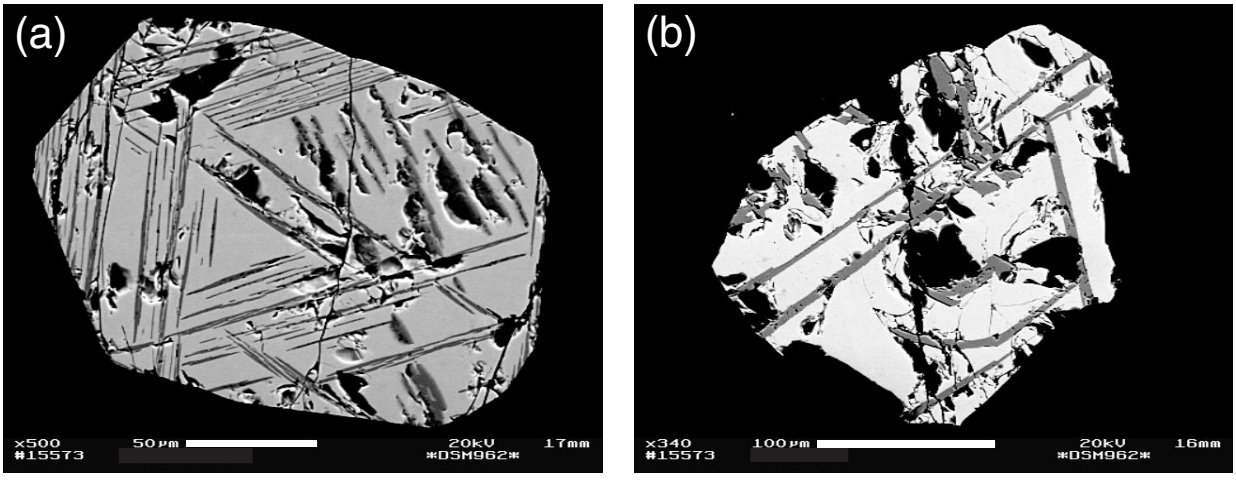

Fig. 9. BSE images of typical magnetite grains showing both fine ilmenite exsolution lamellae (SD20-285) (a) and coarse ilmenite exsolution lamellae (SD45-660) (b).

microprobe error. The orthopyroxene is also characterized by extremely low Al contents (mean Al_2O_3 content is 0·4 oxide wt %; Table A7).

Fe–Ti oxides, sulphides, and graphite

Oxide minerals also show indications of certain systematic changes along the traverse. Within the first 100 cm of the dehydration zone outwards from the pegmatoid dyke, ilmenite is the only Fe–Ti oxide. Chemically, the ilmenite is more enriched in Mn in the vicinity (≈100 cm) of the pegmatoid dyke than further away (Table A8). It contains a moderate hematite component (4–8 oxide wt % Fe_2O_3) and, subsequently, no hematite exsolution lamellae. Modal amounts of ilmenite per sample are constant throughout the traverse and show no particular relationship with respect to the biotite.

Magnetite first appears at ≈100 cm. A minority of the magnetite grains contain trellis-like exsolution lamellae of ilmenite. These tend to be very fine and numerous in magnetite grains from the dehydration zone (Fig. 9a) whereas in the granitic gneiss, these lamellae tend to coarsen (Fig. 9b). Compositionally, the magnetite is near end-member, with relatively minor amounts (<1 oxide wt %) of Cr, Mn, Ti, and Mg. Ilmenite exsolution lamellae in the magnetite–ilmenite grains are enriched in Mn compared with individual ilmenite grains (Table A8). Reintegration of the magnetite–ilmenite grains indicates an original ulvöspinel component of about 20 ± 3%, or $X_{Usp} = 0{\cdot}15 \pm 0{\cdot}03$ ($n = 20$).

Graphite, chalcopyrite, pyrrhotite, and late-stage pyrite occur sporadically in both the dehydration zone

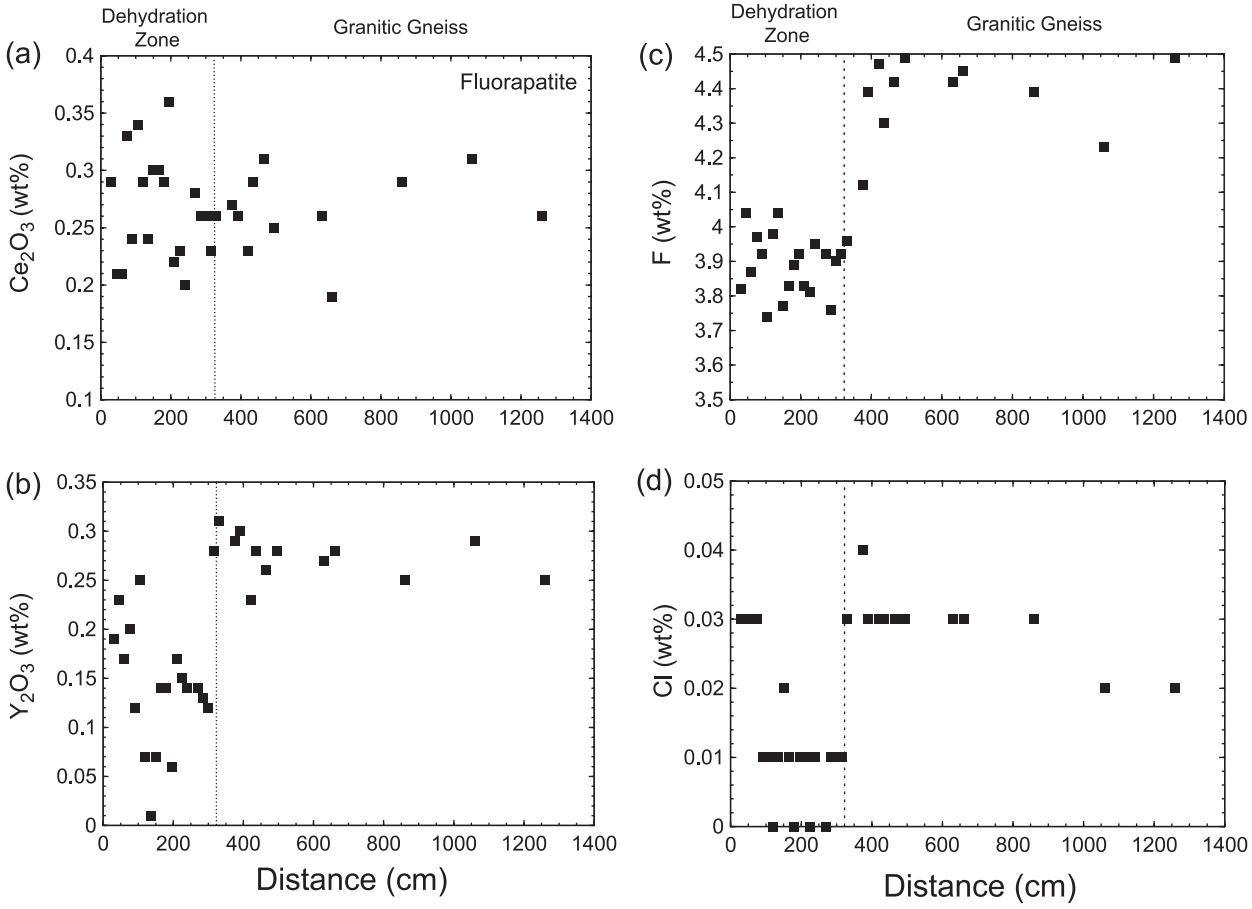

Fig. 10. Plot of fluorapatite chemistry as a function of distance along the traverse outwards from the centre of the pegmatoid dyke for Ce_2O_3 (a), Y_2O_3 (b), F (c), and Cl (d). Dotted line designates the approximate boundary between the dehydration zone and the granitic gneiss. The first symbol in the plot designates the boundary with the pegmatoid dyke.

as well as in the granitic gneiss. Molybdenite is a rare accessory phase in the pegmatoid dyke.

Fluorapatite

Fluorapatite is ubiquitous throughout the dehydration zone and the granitic gneiss and does not contain monazite or xenotime inclusions or rim grains (Table A9; Fig. 10). LREE abundances are relatively constant across the traverse (Fig. 10a). In contrast, mean Y abundances in the fluorapatite (within EMP error) are lower in the dehydration zone than in the granitic gneiss (Fig. 10b) reflecting what is seen in garnet. Similar to both biotite and amphibole, fluorapatite in the dehydration zone has a relatively lower F content compared with fluorapatite in the granitic gneiss, although the change from lower to higher F is abrupt at the boundary between the two zones (Fig. 10c). In contrast, Cl shows more variation, with some indications of enrichment in the immediate vicinity of the pegmatoid dyke and depletion through the remaining dehydration zone compared with fluorapatite in the granitic gneiss, where it suddenly assumes a higher, constant value (Fig. 10d).

Allanite

Allanite forms two morphological populations, both with a similar mineral chemistry, which show no change either in morphology or in relative abundances across the dehydration zone into the granitic gneiss. Population-I consists of small (5–20 μm), relatively homogeneous, anhedral to semi-euhedral grains, which occur in all samples along the traverse (Table A10a). Population-I allanite is commonly associated with fluorapatite, either as discrete grains along the fluorapatite rim or as inclusions. More rarely, allanite is associated with zircon. Typically, the larger Population-I allanite shows faint zoning under back-scattered electron (BSE) imaging, with the brighter rims showing some enrichment in (Y + REE) compared with the darker cores. Population-II consists of large, anhedral, inhomogeneous, mottled grains surrounded by long radiating cracks enriched in LREE, which are visible both in hand sample (Fig. 2d)

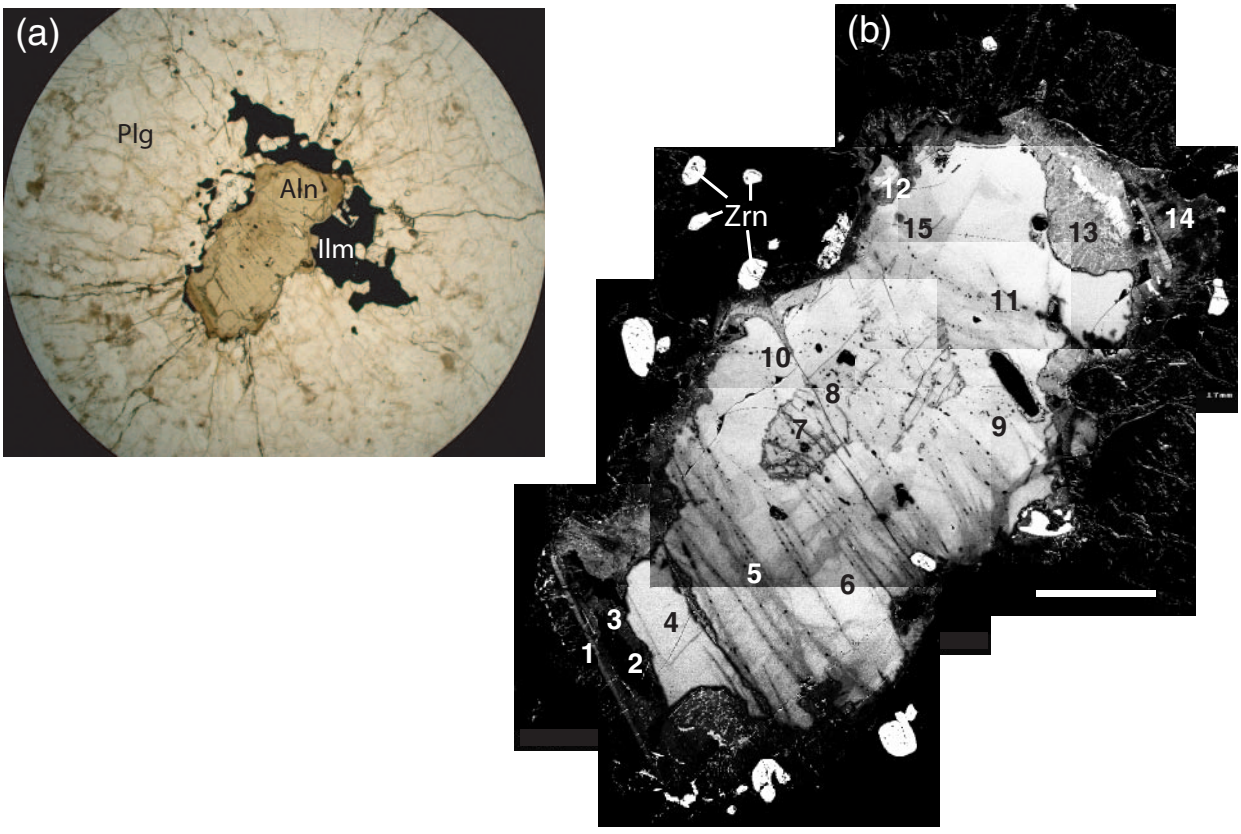

Fig. 11. Large allanite grain typical of both the dehydration zone and the granitic gneiss (see Fig. 2d) in thin section via transmitted light (a) and as a BSE map (b). The radiating cracks surrounding the allanite grain in (a) should be noted. Numbers in (b) refer to allanite analysis points listed in Table A10b.

and thin section (Table A10b; Fig. 11a). Population-II allanite is generally surrounded by numerous grains of zircon and ilmenite (Fig. 11b).

Over the entire traverse, allanite displays variable degrees of alteration. This alteration is manifested by analytical totals below 100% and the presence of some F. Deviations in analytical totals are probably related to the presence of OH and some trivalent Fe. Locally, some of the allanite has undergone more extensive alteration to parisite-(Ce), $Ca(Ce,La,Nd)_2(CO_3)_3F_2$, which shows up more brightly in the BSE image than unaltered allanite. Parisite-(Ce) is intimately intergrown with precursor allanite, hampering reliable analyses of pure material.

ESTIMATION OF TEMPERATURE, PRESSURE, OXYGEN FUGACITY, AND H_2O ACTIVITY

Because of the ubiquity of garnet throughout the traverse, temperatures could be estimated using a variety of Fe–Mg exchange thermometers involving garnet and a series of Fe–Mg silicate minerals. These included garnet–orthopyroxene (Lee & Ganguly, 1988), garnet–clinopyroxene (Berman *et al.*, 1995), garnet–biotite (Holdaway *et al.*, 1997), and garnet–hornblende (Graham & Powell, 1984). Temperatures were also estimated using the Fe–Mn garnet–ilmenite exchange thermometer of Pownceby *et al.* (1991). In the estimation of either temperature or pressure, only mineral core analyses were used. Because of the low Al content in the orthopyroxenes (0·4 oxide wt% Al_2O_3; Table A7), correction for retrograde Fe–Mg exchange between orthopyroxene and garnet (Pattison *et al.*, 2003) adjusted temperatures upwards, on average, only 10°C, well within both analytical and statistical error of the uncorrected Fe–Mg orthopyroxene–garnet temperatures. Disequilibrium between the plagioclase and K-feldspar ruled out the use of two-feldspar thermometry (e.g. Fuhrman & Lindsley, 1988). Pressures were estimated using the assemblage garnet–orthopyroxene–plagioclase–quartz (Harlov, 2000*a*) utilizing mineral thermochemical data from Berman (1988). Fe–Mg–Mn–Ca mixing in garnet is assumed to approximate the model of Berman (1990). As Fe–Mg mixing in garnet is presumed to closely approximate ideality, Fe–Mg experimental K_D exchange data (e.g. Lee & Ganguly, 1988) then require that Fe–Mg mixing in orthopyroxene must approximate ideality as

Table 1: Temperatures and HF and HCl fugacities relative to H_2O

Sample	Zone	Gt–Opx *T**	Gt–Cpx *T*†	Gt–Bt *T*‡	Gt–Am *T*§	$\log(f_{H_2O}/f_{HF})$	$\log(f_{H_2O}/f_{HCl})$	$\log(f_{HF}/f_{HCl})$
SD3-30	Cpx		655	655		4·29	3·95	−0·34
SD4-45	Cpx		660	630	590	4·42	4·04	−0·38
SD5-60	Cpx		595	690	485	4·40	4·13	−0·28
SD6-75	Cpx		645	670	580	4·29	4·14	−0·15
SD7-90	Opx + (Cpx)	640	655	725	605	4·25	4·50	0·25
SD8-105	Opx + (Cpx)	605		750	595	4·29	4·58	0·29
SD9-120	Opx + (Cpx)	570	610	740	605	4·30	4·53	0·24
SD10-135	Opx + (Cpx)	650		815	650	4·27	4·28	0·01
SD11-150	Opx + (Cpx)	640		735		4·28	4·19	−0·09
SD12-165	Opx + (Cpx)	630	695	735	605	4·30	4·58	0·28
SD13-180	Opx + (Cpx)	650	725	750	610	4·24	4·64	0·41
SD14-195	Opx + (Cpx)	635	675	735	605	4·24	4·68	0·44
SD-15-210	Opx + (Cpx)	610	665	650	625	4·25	4·59	0·34
SD16-225	Opx + (Cpx)	595	665	725	590	4·27	4·63	0·36
SD17-240	Opx + (Cpx)	630	680	700	605	4·23	4·60	0·37
SD19-270	Opx + (Cpx)	625	705	745	600	4·24	4·51	0·26
SD20-285	Opx + (Cpx)	635		710	620	4·2	4·57	0·37
SD21-300	Cpx		670	625	585	4·17	4·53	0·36
SD-22-315	Cpx		675	705	585	4·14	4·39	0·25
SD23-330	amphibolite			660	600	4·14	3·69	−0·45
SD26-375	amphibolite			675	605	4·09	3·64	−0·45
SD27-390	amphibolite			730	620	4·10	3·76	−0·34
SD29-420	amphibolite			675	590	4·06	3·70	−0·35
SD30-435	amphibolite			730	615	4·06	3·60	−0·45
SD32-465	amphibolite			690	595	4·05	3·61	−0·44
SD34-495	amphibolite			690	620	4·05	3·60	−0·45
SD43-630	amphibolite			695	600	4·02	3·62	−0·40
SD45-660	amphibolite			660	575	4·02	3·60	−0·42
SD45+2-860	amphibolite			690	610	3·94	3·59	−0·35
SD45+4-1060	amphibolite			670	590	3·95	3·62	−0·33
SD45+6-1260	amphibolite			655	585	3·96	3·58	−0·38

*Garnet–orthopyroxene thermometer, Lee & Ganguly (1988).
†Garnet–clinopyroxene thermometer, Berman *et al.* (1995).
‡Garnet–biotite thermometer, Holdaway *et al.* (1997).
§Garnet–amphibole thermometer, Graham & Powell (1984).

well. Again, because of the low Al_2O_3 content, effects of Al mixing in orthopyroxene were assumed to be negligible. Ca–Na–K mixing in plagioclase was approximated using the plagioclase mixing model of Newton (1983).

In the dehydration zone, utilizing the mineral chemistry documented in Tables A3–A8, garnet–orthopyroxene thermometry indicates a mean temperature of 624 ± 23°C (1σ) (n = 13), whereas garnet–clinopyroxene thermometry gives a mean temperature of 665 ± 33°C (n = 15) (Table 1). Across the breadth of the traverse, garnet–biotite thermometry indicates a mean temperature of 700 ± 42°C (n = 31) and garnet–hornblende thermometry gives a mean temperature of 598 ± 27°C (n = 29) (Table 1). Lastly, garnet–ilmenite thermometry indicates a mean temperature of 567 ± 67°C (n = 31). Starting at the boundary with the pegmatoid dyke, no gradation in temperature is seen across the traverse for any of the five thermometers utilized, i.e. outside their published error bars (see Table 1).

Assuming that the garnet–orthopyroxene, garnet–clinopyroxene, and garnet–biotite thermometers have the highest blocking temperatures (Berman *et al.*, 1995; Holdaway *et al.*, 1997; Pattison *et al.*, 2003) would suggest

an approximate temperature for the *c.* 1400 Ma dehydration event of 650–700°C. This temperature range is also supported by the relatively low Al_2O_3 content in the orthopyroxene, i.e. 0·4 oxide wt % (e.g. Aranovich & Berman, 1997; see also Nijland *et al.*, 1998; Morishita *et al.*, 2003). Subsequently, garnet–orthopyroxene–plagioclase–quartz barometry indicates a mean pressure range of 750 ± 30 to 820 ± 30 MPa ($n = 13$) or a mean pressure of 785 MPa.

Preservation of element traverses in the mineral chemistry, coupled with the low Al content in the orthopyroxene, argues against overprinting of the mineral cores in the *c.* 1400 Ma dehydration zone or surrounding granitic gneiss during the *c.* 900–1000 Ma Sveconorwegian–Grenvillian orogeny (680–750°C; 850–1050 MPa—Söndrum area; Wang & Lindh, 1996). This particular *PT* range is reflected in orthopyroxene from mafic rocks in the SGR, whose Al_2O_3 content typically range from 1 to 2 wt % (Wang & Lindh, 1996), more than twice that measured for orthopyroxene from the dehydration zone (Table A7). Local evidence for this Sveconorwegian overprint is seen in a nearby granulite-facies metadolerite dyke, where the orthopyroxene has an Al_2O_3 content of 1·3 wt % (Fig. 1c; Table A7). Here, garnet–orthopyroxene and garnet–clinopyroxene thermometry indicate a temperature of 720°C and a subsequent pressure (garnet–orthopyroxene–plagioclase–quartz) of 770 MPa; both in good agreement with the *PT* range determined by Wang & Lindh (1996).

Oxygen fugacity was estimated using the assemblage ferrosilite–magnetite–quartz in those samples containing orthopyroxene (see Harlov, 1992, 2000*b*). For purposes of internal consistency, Fe–Mg mixing in orthopyroxene was approximated using the mixing model of Sack & Ghiorso (1989), whereas the composition of the magnetite is assumed to represent a near end-member composition. Assuming a mean temperature and pressure of 700°C and 800 MPa, respectively, results in a mean $\log(f_{H_2O})$ of −15·56 ± 0·04 bars ($n = 13$). If the subset of magnetite grains, with an ulvöspinel component ($X_{Usp} = 0{\cdot}15 \pm 0{\cdot}03$), is utilized in the estimation of ferrosilite–magnetite–quartz oxygen fugacities instead, a mean $\log(f_{O_2})$ of −15·66 ± 0·04 bars ($n = 13$) is obtained, in close agreement with the oxygen fugacity estimated using end-member magnetite. Here, the magnetite activity was estimated using the formulation and graphs of Sack & Ghiorso (1991*a*, 1991*b*) and Ghiorso & Sack (1991). At 700°C and 800 MPa, these numbers indicate an oxidation state *c.* 0·8 log units above the graphite stability curve, and 0·7 log units above the fayalite–magnetite–quartz equilibrium (see Frost, 1991; Harlov, 1992, 2000*b*). This would imply that the sporadic occurrence of graphite is late-stage, having been deposited after the metamorphic dehydration event, and thus is probably secondary.

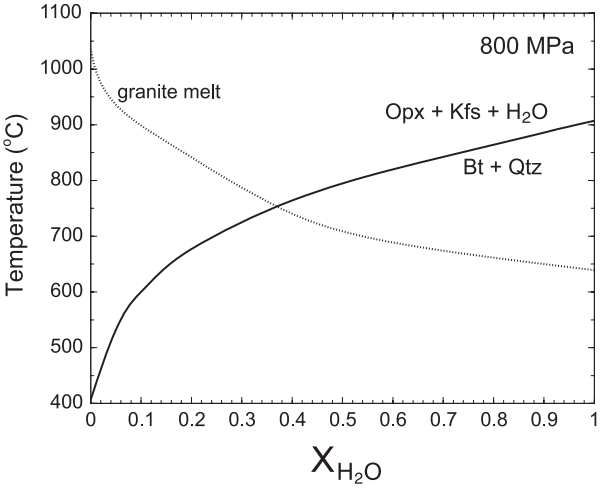

Fig. 12. T–X_{H_2O} plot at 800 MPa of the granite melting curve inferred from the experimental data of Ebadi & Johannes (1991) and the biotite–quartz–orthopyroxene–K-feldspar–H_2O equilibrium calculated using the THERMOCALC program (Holland & Powell, 1998; Powell *et al.*, 1998) for mean values of K-feldspar, biotite and orthopyroxene taken from orthopyroxene-bearing samples in Tables A2b, A3, and A7, respectively.

A mean H_2O activity and X_{H_2O} were estimated from reaction (2) by incorporating the averaged orthopyroxene, biotite and K-feldspar analyses from Tables A2b, A3, and A7 for orthopyroxene-bearing samples ($n = 12$) into the THERMOCALC program of Powell *et al.* (1998) (see also Holland & Powell, 1998). Assuming a representative temperature and pressure of 700°C and 800 MPa, respectively, results in an H_2O activity of 0·36 and subsequent X_{H_2O} of 0·25. When the H_2O activity is estimated for individual mineral analyses per sample, despite some scatter, no obvious gradient in the H_2O activity is seen across the dehydration zone (Table 1). If X_{H_2O} is calculated as a function of temperature at 800 MPa for reaction (2), using these averaged mineral compositions, this equilibrium can be plotted vs temperature in T–X_{H_2O}–X_{CO_2} space (Fig. 12). Also plotted is the granite melting curve at 800 MPa approximated from the experimental data of Ebadi & Johannes (1991). At 700°C and 800 MPa, an X_{H_2O} of 0·25 plots well into the stability field for granite, implying that partial melting could not have taken place during the dehydration event and thus supporting the contention that conversion of amphibole and biotite to pyroxene occurred under solid-state conditions.

FLUID INCLUSIONS

Fluid inclusions from eight samples along the traverse were studied (see Fig. 2b for sampling sites). These included one from the pegmatoid dyke (SD1-0), five from the dehydration zone (SD3-30, SD4-45, SD8-105, SD15-210, SD22-315), and two from the granitic gneiss

(SD26-375, SD34A-495). Fluid inclusions were found only in quartz, where they occur as isolated inclusions, in clusters, or in a planar arrangement. The fluid inclusions are classified as (1) aqueous inclusions and (2) CO_2-bearing inclusions. Members of these groups occur in all samples throughout the traverse, with relative abundances varying with respect to the different lithologies.

Aqueous inclusions

Two distinct population groups can be distinguished among the aqueous inclusions. These include low-salinity aqueous inclusions and saline aqueous inclusions with a maximum of 18 wt % equivalent NaCl. Solid phases in the fluid inclusions are rare and correspond to accidentally trapped phases or secondary carbonate.

Low-salinity aqueous inclusions

The low-salinity aqueous inclusions are by far the most abundant and occur mostly in healed fractures. This indicates the late introduction of almost pure water into the rock system. These inclusions are often monophase at room temperature, with many inclusions losing their bubbles on freezing. They have densities close to that of ice (0·917 g/cm^3) and show homogenization temperatures (T_h) normally above about 150°C, though a few show T_h of more than 200°C (Fig. 13). The highest T_h for pure water is about 320°C. Although monophase inclusions are abundant in most samples, only a few of them produce bubbles on cooling and show subsequent homogenization always below 150°C (Fig. 13).

So-called 'stretched' fluids in monophase inclusions remain in tension until bubble nucleation. Ice melting in 'stretched' water without a bubble (S + L → L) may take place above 0°C, with the bubble often appearing at or just after ice melting. 'Non-stretched' monophase inclusions (higher density) melt at lower temperatures than 'normal'; that is, along the melting (S + L) line. As a consequence, melting temperatures as low as −7°C are sometimes observed for apparently pure water inclusions.

Saline aqueous inclusions

Saline aqueous inclusions are more abundant in samples with higher-density, carbonic, and aqueous–carbonic inclusions. The saline aqueous inclusions occur in clusters, or sometimes in short trails, which locally, on the micron scale, have the same salinity as the inclusions in the clusters. This suggests the local shearing and retrapping of fluids along new-formed fractures. Larger saline aqueous inclusions in the same healed fracture may have a somewhat higher salinity compared with the smaller inclusions. Furthermore, larger inclusions usually show a lower density, whereas smaller inclusions show a higher density. These observable facts can be explained by the retrapping of immiscible fluids.

Eutectic melting temperatures (T_m) are typically about −22°C, indicating that the brines are NaCl-dominated. High-salinity inclusions (X_{NaCl} = 15–18 wt %) have T_h <130°C. The high-salinity inclusions also have a lower T_h compared with pure water (Fig. 14).

CO_2-bearing inclusions

Two groups of CO_2-bearing fluid inclusions can be distinguished. These include aqueous–carbonic inclusions (H_2O–NaCl–CO_2) and essentially pure carbonic inclusions.

Aqueous–carbonic inclusions

Although rare, aqueous–carbonic inclusions are present in most of the samples. Some inclusions with 'primary' characteristics occur in the dehydration zone (e.g. SD15-210). These are relatively large (10–20 μm) inclusions in clusters, with regular morphologies and water fill degrees of about 0·5 (Fig. 15a). However, in other samples, the degree of fill varies between 0·1 and 0·7. The inclusions occur in relatively non-disturbed micro-domains, between sharp trails of pure water inclusions. The systematic higher density [up to about 0·9 g/cm^3 (T_hL = −3°C)] for CO_2 in the aqueous–carbonic inclusions is obvious compared with the non-aqueous carbonic inclusions in the same sample.

Rare observations of ice melting between −4 and −6°C correspond to salinities of 7–9 wt % NaCl. Clathrate hydrate melting at 6–8°C for salinities of 4–8 wt % NaCl was observed in a few of the fluid inclusions.

Carbonic inclusions

Carbonic inclusions often occur in clusters with disordered textures (Fig. 15b). Other inclusions occur in sharp trails (Fig. 15c) or in planar arrangement (open trails). These CO_2 inclusions are younger than H_2O inclusions, which occur in clusters with an irregular morphology. Fluid inclusion morphologies vary from irregular to rounded and negative crystal shapes, and occur primarily in the trails. These textures are indicative of post peak-metamorphic re-equilibration and re-trapping. The inclusions sometimes contain small amounts of visible water (degree of fill <0·1). The carbonic inclusions show extreme density variation, from apparent 'empty' inclusions (dark appearance in transmitted light and without visible phase transitions) to high-density fluid inclusions of *c.* 0·90 g/cm^3. Only a few carbonic inclusions show bubbles on cooling, with homogenization occurring mostly in the gas phase. However, the vast majority of the 'measurable' inclusions show an approximate critical homogenization; that is, at or just below 31°C, corresponding to a density of about 0·47 g/cm^3. This also implies an essentially pure CO_2 composition. Accordingly, the melting temperature is always close to that of

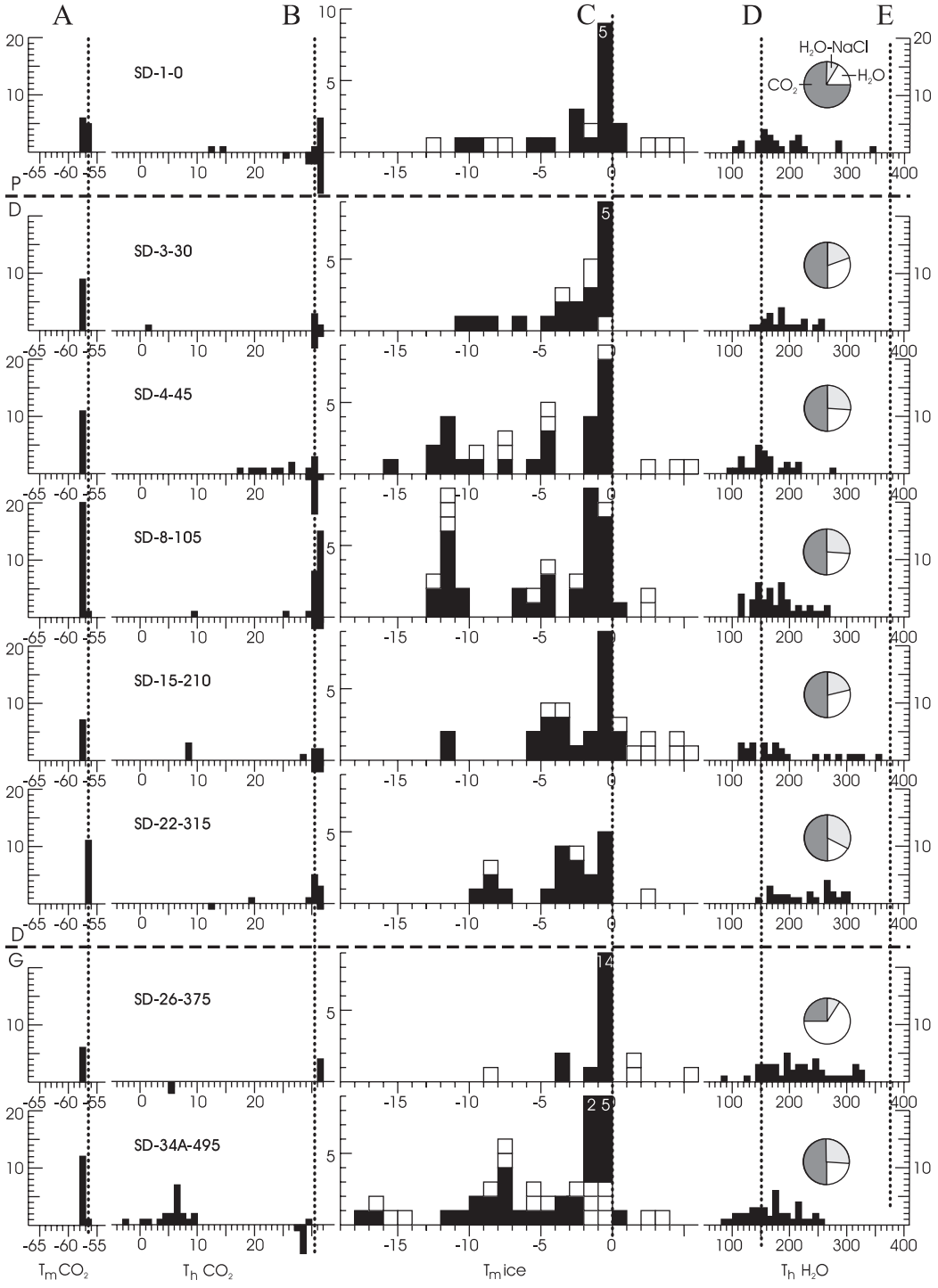

Fig. 13. Microthermometry data for fluid inclusions along the traverse covering the pegmatoid dyke, the dehydration zone, and the granitic gneiss. Horizontal dashed lines signify divisions between the pegmatoid dyke (P), the dehydration zone (D), and the granitic gneiss (G). Frequency distributions are shown for the melting temperature of CO_2 (T_m CO_2), homogenization temperature of CO_2 (T_h CO_2), ice melting temperatures (T_m ice), and homogenization temperatures of aqueous inclusions (T_h H_2O). Pie-diagrams show the estimated relative abundance of carbonic (CO_2), saline aqueous (H_2O–NaCl), and pure water inclusions (H_2O). The homogenization temperature for CO_2 (i.e. T_hCO_2) may be either to the liquid phase (positive values) or to the vapour phase (negative values). White numbers in the histograms indicate measurements, which are not graphically represented. Vertical dotted lines are as follows: A, T_m for pure CO_2 (−56·6°C); B, critical T_h for pure CO_2 (31°C); C, T_m for H_2O (0°C); D, the boundary between monophase (left) and two-phase inclusions (right); E, critical T_h for pure H_2O (374°C). H_2O melting in the histogram is represented as triple-point melting S + L + V → L + V (■) or as metastable melting of 'stretched' fluids S + L → L (□).

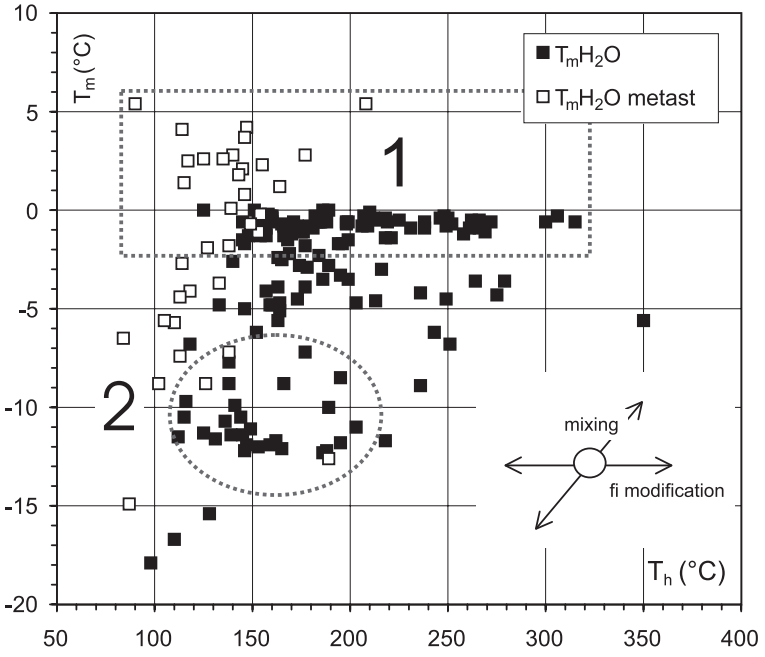

Fig. 14. Melting vs homogenization temperatures (T_m, T_h) for aqueous inclusions. □, Inclusions showing metastable melting (without bubble). Fluid inclusion (fi) modification results in T_h variation, whereas mixing results in varying T_m. 1, Late fluids of almost pure water; 2, early fluids, which are partly produced by the immiscibility of H_2O–CO_2–NaCl fluid and represent pre-existing brines in the granitic gneiss before the dehydration event.

pure CO_2 (−56·6°C). High CO_2 density fluid inclusions are found sporadically in almost all the samples (Fig. 13). However, the best preserved are found in samples that contain abundant high-salinity fluid inclusions, such as those in the granitic gneiss (e.g. SD34A-495 in Fig. 13), and to a lesser extent, those in the central part of the dehydration zone.

Major fluid types in the different zones

The pegmatoid dyke shows the highest abundance of CO_2 inclusions (Fig. 13), which is reflected in the whole-rock analyses (Table A1). The density of these inclusions is generally very low. In addition to the carbonic inclusions, aqueous inclusions also occur but in separate domains. Mixed aqueous–carbonic inclusions are rare.

In the dehydration zone, the relative abundances of aqueous and carbonic inclusions are about equal. The greatest percentage of high-salinity aqueous inclusions occurs about 0·4–1 m from the contact with the pegmatoid dyke (Figs 13 and 16). On the micrometre scale, the carbonic and high-salinity aqueous inclusions tend to be associated in the same domains. In contrast, pure H_2O inclusions occur in trails, mostly in different domains.

The granitic gneiss samples contain well-developed, aqueous and carbonic inclusions. Mixed H_2O–CO_2 inclusions are also rare here. The sample from deep within the granitic gneiss (SD34A-495) contains relatively many aqueous inclusions of high salinity, which are associated with CO_2. On the other hand, only almost pure water inclusions are found in clusters or in healed fractures in the sample of granitic gneiss that borders the contact with the dehydration zone (SD26-375) (Fig. 13). Here, CO_2 inclusions are almost absent. Some parallel trails of low-density, or 'empty' CO_2 inclusions, indicate strong deformation and/or shearing in this zone.

INTERPRETATION OF MINERAL TEXTURES AND CHEMISTRY

Feldspar–quartz mineral textures and chemistry in the dehydration zone are identical to those in the surrounding granitic gneiss, implying that the fluids responsible for the partial conversion of biotite and amphibole to orthopyroxene and clinopyroxene via reactions (1) and (2) had no obvious effect on either (Fig. 4a and c; Table A2). Enrichment in Na along plagioclase grain rims in contact with K-feldspar (Fig. 4b and d), apparent myrmekitic intergrowths of quartz and plagioclase (Fig. 4e), as well as mesoperthite (Fig. 4f), all point to some sort of interaction with either a fluid or a fluid-rich melt, probably with an NaCl brine component. This probably occurred during the regional, 1420–1460 Ma migmatization event, as such textures are also found in the granitic gneiss throughout the SGR.

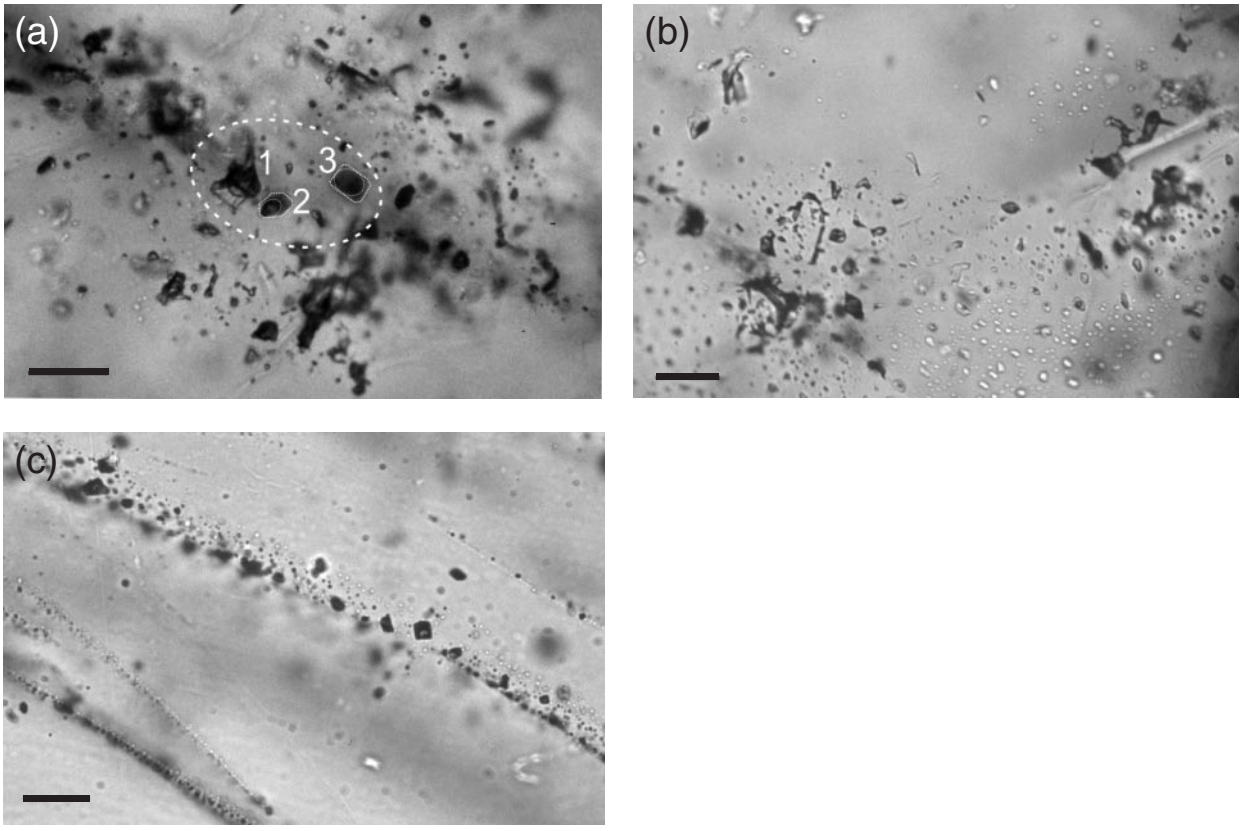

Fig. 15. (a) (SD15-210) A domain with primary inclusions surrounded by strongly modified inclusions and fluid inclusion trails. The inclusions, which are out of focus, are outlined. The three inclusions indicated have water-filling degrees of 0·3–0·5. The CO_2 homogenization (to liquid) is +8°C for the three inclusions; T_m ice for inclusion 1 is −4·5°C, T_m clathrate is + 8·4°C. (b) (SD15-210) Two decrepitated clusters of CO_2 inclusions with irregular shapes and smaller aqueous inclusions showing bubbles. (c) (SD8-105) Sharp trails of pure CO_2 inclusions. Scale bar represents 25 μm in all photographs.

One feature common to the Fe–Mg silicate minerals and ilmenite is the strong partitioning of Mn and Mg into, and Fe out of, these minerals in the first 100–150 cm of the dehydration zone (Figs 5b, c; 6b, c; and 7). Such a phenomenon cannot be interpreted as having resulted from an imposed high oxidation state (e.g. Harlov *et al.*, 1997), as magnetite has been removed and ilmenite has lost Fe. Rather, fluids in the first 100–150 cm of the dehydration zone must have had a high affinity for Fe, influenced by the fluid-rich granitic melt responsible for the pegmatoid dyke, which acted as chemical sink for Fe, such that the Fe was then removed from the general locality. This is supported by the fact that the pegmatoid dyke is low in Fe relative to the granitic gneiss (Table A1). This chemical affinity for Fe was apparently strong enough to influence the chemistry of Fe–Mg silicate minerals *c.* 100–150 cm into the surrounding dehydration zone, such that the chemical potentials favoured the partitioning of Fe into the CO_2–NaCl–H_2O grain boundary fluids present, which subsequently aided the mobility of Fe towards the granitic melt.

Both biotite and amphibole show relatively uniform enrichment in Ti in the dehydration zone (Figs 5a and 6a), which would appear to indicate that the dehydration event itself was characterized by advective transport. Titanium enrichment in biotite is common in both localized and well as regional dehydration zones; that is, regions that have undergone granulite-facies metamorphism to orthopyroxene-bearing rocks (e.g. Hansen *et al.*, 2002; Harlov & Förster, 2002*a*). In either case, Ti enrichment appears to be related to reactions (1) and (2), which free up Ti to be absorbed by the remaining biotite and amphibole, thereby stabilizing both minerals against conversion to pyroxenes. This would also explain why enrichment of biotite and amphibole in Ti is directly correlated with the formation of orthopyroxene and clinopyroxene. With respect to the amphiboles, enrichment in Ti certainly cannot be ascribed as a function of increasing temperature across the traverse (e.g. Ernst & Liu, 1998).

Correlation between Ti in biotite and the metamorphic 'grade', as it relates to the presence or absence of

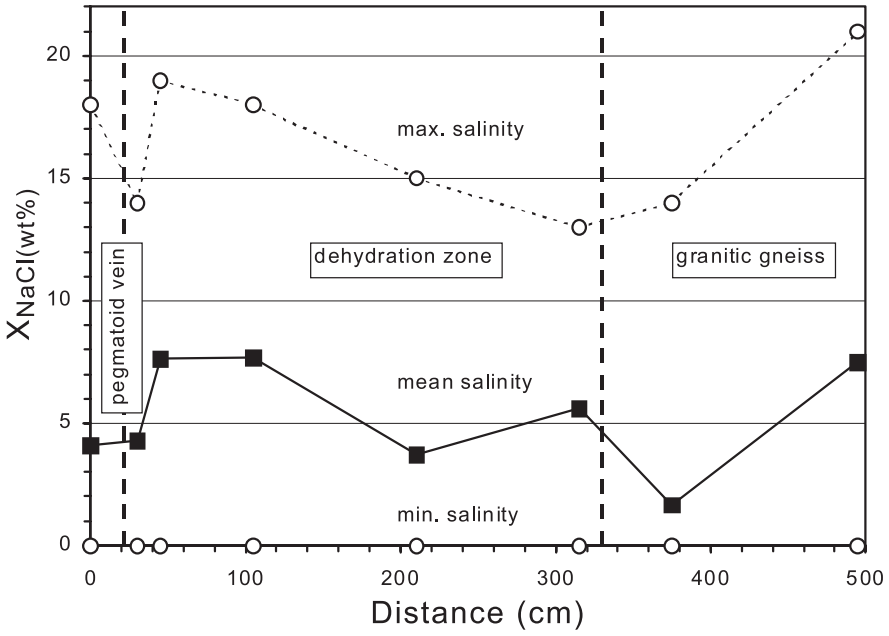

Fig. 16. Mean and maximum salinity of fluid inclusions (expressed as X_{NaCl}, in wt %) along the traverse.

orthopyroxene, agrees well with experiment (e.g. Patiño-Douce, 1993). Patiño-Douce (1993) demonstrated experimentally that the solubility of Ti in biotite increases with temperature in a strongly non-linear fashion such that up to amphibolite-facies conditions, the effect of Ti on the stability of biotite is very small. However, upon initiation of the dehydration reactions associated with granulite-facies metamorphism and the lower H_2O activities that characterize it, Ti in biotite increases markedly, rendering the biotite relatively refractory. Recently, Ti enrichment in biotite, as a function of increasing metamorphic grade, has been empirically calibrated as a geothermometer for high-grade metapelites using extensive natural biotite data (Henry *et al.*, 2005).

In a similar manner, Ca enrichment in the remaining amphiboles in the dehydration zone (Fig. 6d) is also an indicator of advective transport. In the most likely scenario, a portion of this Ca, released during amphibole breakdown, would be taken up by the formation of clinopyroxene. However, because of the paucity of clinopyroxene across a large portion of the dehydration zone, the majority was apparently partitioned back into the remaining amphibole, subsequently forcing out Na and, to a lesser extent, K, such that charge balance was maintained (Fig. 6e and f). Sodium and K were apparently either flushed out of the dehydration zone or, more probably, partitioned into the feldspars, whose high Na and K content allows them to be treated as an infinite reservoir with respect to the absorption of such relatively minor amounts of Na and K. Steep Na and K depletion in amphiboles in the first 100 cm out from the pegmatoid dyke (Fig. 6e and f) appears to mirror the equally dramatic depletion in Fe seen in the Fe–Mg silicates in general. This suggests that they might be coupled in some way, perhaps as a result of increased mobility of a brine component along grain boundaries during either the formation or the crystallization of the granitic melt responsible for the pegmatoid dyke.

Biotite, amphibole, and fluorapatite halogen chemistry

In the dehydration zone, all three halogen-bearing minerals (i.e. biotite, amphibole, and fluorapatite) show depletion in F and Cl (Figs 5d–f; 6g, h; and 10c, d). Depletion in Cl is limited to the dehydration zone, with a sharp cut-off at the boundary with the granitic gneiss, thus suggesting that its depletion was also a product of advective transport. This indicates that the Cl was partitioned into the low H_2O activity fluid responsible for the dehydration event and subsequently moved out of the dehydration zone via advective transport. What is apparently only a partial depletion in Cl in the first 100 cm out from the pegmatoid dyke, relative to the rest of the dehydration zone, could be explained as being due to the expulsion of Cl during the last phases of crystallization of the granitic melt responsible for the pegmatoid dyke. Such a phenomenon is common in crystallizing, deep-seated melts under similar, granulite-facies conditions (e.g. Markl & Piazolo, 1998).

In contrast, whereas F is uniformly depleted in fluorapatite, with a relatively sharp cut-off at the boundary with the granitic gneiss again indicative of advective transport, the F component in biotite and amphibole shows a more

gradual transition across this boundary. This behaviour indicates that F depletion in the silicate minerals continued deep into the granitic gneiss, without conversion of biotite and amphibole to pyroxenes, or depletion of garnet and fluorapatite in HREE (Figs 8, 10a and b). Such a convex curve documenting depletion in F in either biotite or amphibole as a function of distance from an apparent sink for F, represented by the central fluid-rich granitic melt responsible for the pegmatoid dyke, essentially mirrors that of a concentration gradient following Fick's Second Law or

$$\frac{\partial c}{\partial t} = D\frac{\partial^2 c}{\partial x^2} \quad (3)$$

where c is concentration, t is time, D is the diffusion coefficient, and x is the direction of the concentration gradient. Here, the shape of the F curve indicates that $(\partial^2 c/\partial x^2) < 0$, which would imply that F diffused along the concentration gradient towards the granitic melt.

This observation results in two inferences: (1) a continuous fluid medium existed along grain boundaries throughout both the dehydration zone and the surrounding granitic gneiss and (2) F was partitioned from the biotite and amphibole into this fluid and subsequently diffused along grain boundaries towards the granitic melt. This would imply that biotite and amphibole were in disequilibrium with the fluid in their immediate neighbourhood such that F was preferentially and continuously in the process of being partitioned from either mineral into this fluid. The pattern in biotite and amphibole F concentrations currently seen along the traverse would then represent a mirror of the concentration gradient existing in the fluid along grain boundaries at the point, when the granitic melt had completely crystallized to the pegmatoid dyke. These patterns would imply that the granitic melt acted as a natural sink for F. If true, the low F abundances in the pegmatoid dyke relative to the surrounding rock seen today (Table A1) would further imply that the granitic melt–tectonic fracture must have been an open system continually replenished by F-poor fluids such that F, diffusing in from the surrounding rock, was continually being diluted in this fluid-rich melt and removed, presumably to higher levels up along the rock column.

Trace element mineral chemistry

Despite having a sufficiently large (Y + REE) budget [i.e. $(Y + REE)_2O_3$ of 0·5–1·0 wt %; see Harlov & Förster (2002*b*)], monazite and xenotime inclusions or rim grains associated with fluorapatite did not form during dehydration of the amphibolite-facies gneiss. In addition, fluorapatite shows no depletion in LREE nor does Population-I or -II allanite, with the exception of rare low-grade parisite-(Ce), show any alteration. In contrast, measurable depletion of Y in fluorapatite (Fig. 10b) from the dehydration zone, coupled with depletion of (Y + HREE) in the garnet (Fig. 8) as well as in the whole-rock analysis (Table A1; Fig. 3), indicates that these elements were highly mobile in the same fluids responsible for the partial conversion of biotite and amphibole to pyroxenes. Both experimentally and in nature, (Y + HREE) are known to preferentially complex with the F, whereas LREE preferentially complex with Cl (Haas *et al.*, 1995; Pan & Fleet, 1996). The most likely scenario would be leaching of (Y + HREE) from the fluorapatite and garnet to complex with the F released during the partial conversion of biotite and amphibole to orthopyroxene and clinopyroxene as well as F partitioned out of the remaining biotite and amphibole and out of the fluorapatite. As a consequence, migration of F from the dehydration zone into the fluid-rich granitic melt responsible for the pegmatoid dyke would then deplete the dehydration zone in (Y + HREE). Lastly, lack of monazite and xenotime associated with fluorapatite, coupled with Cl depletion, puts constraints on the fluid to one containing CO_2 and NaCl components, but not dominated by $CaCl_2$ or KCl (Harlov & Förster, 2003), which agrees both with the fluid inclusion data as well as with the feldspar mineral chemistry.

INTERPRETATION OF FLUID INCLUSION DATA

Fluid compositions and densities, combined with textural information, delimit the trapping conditions and the relative timing for each of the fluid types during rock evolution. Hence, the pure H_2O fluids, typically trapped in healed fractures and evidently late, must be unrelated to the dehydration event. On the other hand, the high-salinity brines are clearly earlier than pure H_2O. These early fluids can be interpreted as (1) the original magmatic fluid inherent to the granitic gneiss, which originated during the migmatization event (*c.* 1420–1460 Ma), and was probably collected by an uptake of water in the melt during migmatization of the granitic gneiss, and/or (2) brines produced by the unmixing of aqueous–carbonic fluids in the dehydration zone.

The construction of isochores allows for the possibility of determining the *PT* conditions present during fluid trapping, and subsequent comparison with *PT* estimates obtained from mineral thermobarometry. Isochores have been calculated from microthermometry data using the FLUID package of Bakker (2003). Figure 17 shows the isochores of selected fluid inclusions, together with a selection of metamorphic *PT* conditions.

Identification of the dehydration fluid

The poorly preserved H_2O–CO_2–NaCl inclusions (see Fig. 15a) are identified as the dehydrating fluid. This

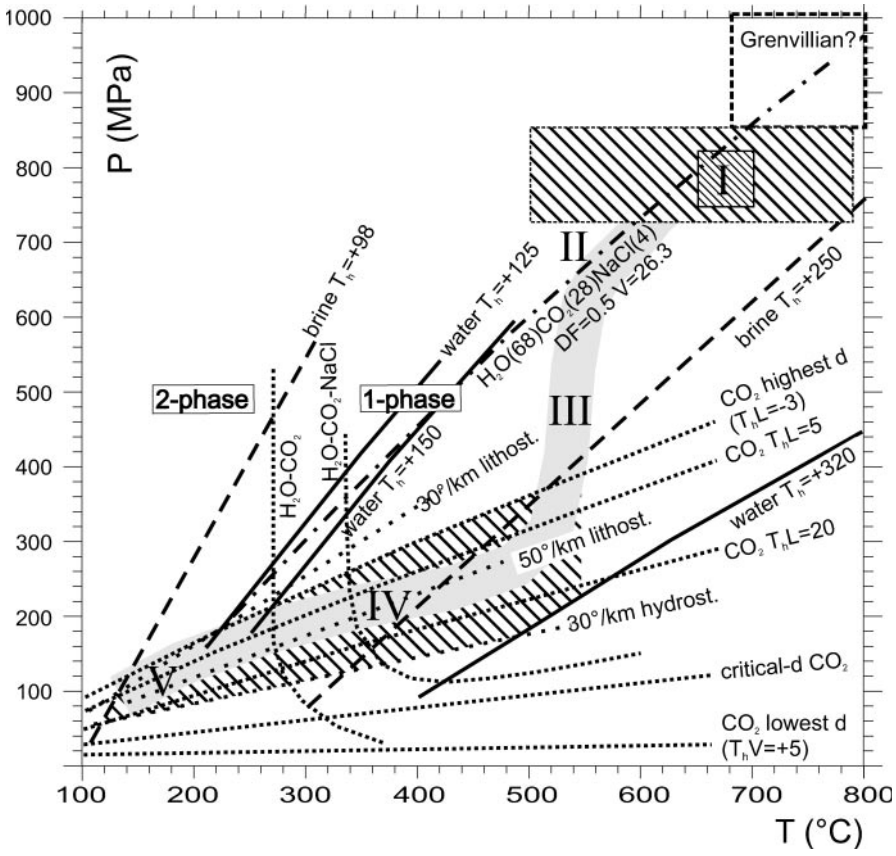

Fig. 17. Representative isochores for the main fluid inclusion compositions: carbonic, aqueous (water or brine), and aqueous–carbonic inclusions. The shaded boxes indicate the metamorphic conditions during the dehydration event as revealed by the mineral chemistry. The larger box shows the maximum ranges implicit to the accuracy of the different mineral geothermobarometers. The retrograde uplift path is in part characterized by isothermal decompression (lithostatic). The earliest recognizable fluid is characterized by an H_2O–CO_2–NaCl composition. An example of such fluid inclusions is shown in Fig. 15a. Near-isothermal uplift resulted in the decrepitation of fluid inclusions under conditions of aqueous–carbonic immiscibility (e.g. Fig. 15b). The latest part of the uplift path must have graded towards the 30°/km lithostatic gradient. Here, evidence was found for the admixing of pure water at temperatures below about 500°C. Implosion decrepitation resulted in progressive higher densities of the aqueous inclusions, whereas the CO_2-rich inclusions must have lost the water as a result of partial leakage along microfractures (e.g. Fig. 15c). Geothermal gradients are given for 30°/km (lithostatic and hydrostatic) and for 50°/km (lithostatic). Miscibility limits are shown for salt-free H_2O–CO_2 and for H_2O–CO_2–NaCl (6 wt % NaCl relative to the NaCl subsystem and 21 mol % CO_2; Krüger & Diamond, 2001). (I) represents the peak of metamorphism characterized by local dehydration owing to the introduction of H_2O–CO_2–NaCl fluids from the initial tectonic fracture responsible for the dehydration zone in the granitic gneiss. Brines originating from the magmatic stage were probably already present (and in part preserved) in the granitic gneiss, but these fluids were immiscible with the dehydration fluid. (II) represents a more or less isochoric uplift, which left the trapped brines and dehydration fluids largely unchanged. (III) represents an almost isothermal uplift (dropping pressures) resulting in the decrepitation of fluid inclusions, almost directly followed by fluid unmixing and retrapping represented by (IV). During this stage, the salinity of the aqueous fluids was reduced and the density of CO_2 lowered. However, the higher-salinity and carbonic inclusions remained in close association. During final cooling, almost pure water was introduced into the system and in part disturbed the original contrasting fluid compositions. Retrapped water inclusions show progressive higher density (monophase). Carbonic inclusions with small amounts of water may have reduced their density as a result of water leakage.

interpretation is supported both by the observation that CO_2-rich fluids are dominant in the pegmatoid dyke as well as by the position of the corresponding isochore, which demonstrates that the possible trapping conditions for H_2O–CO_2–NaCl inclusions with a fill degree of around 0·5 concur with the estimated *PT* conditions (650–700°C and 750–820 MPa) present during the dehydration event [e.g. the $H_2O(68)$–$CO_2(28)$–NaCl(4) isochore in Fig. 17]. At these temperatures and pressures, the aqueous–carbonic fluid inclusions are homogeneous and would represent one possible means of transport for CO_2, namely as a part of a supercritical fluid mixture. This would explain the high CO_2 density currently seen in the carbonic fraction. In the dehydration zone, the H_2O–CO_2–NaCl fluids are relatively well preserved, suggesting near-isochoric uplift in the fluid miscibility field followed by fluid immiscibility towards lower temperatures. The latter conditions have resulted in the formation of the closely associated carbonic and brine inclusions.

As the source of the dehydration fluid is obviously the pegmatoid dyke, it is strange that aqueous–carbonic fluid inclusions are apparently rare here. This near absence would suggest that these fluids must have been expelled from the pegmatoid dyke before the end of its magmatic stage. However, the *PT* conditions were not sufficient to induce melting of the surrounding rock. In such a situation, the reactive potential of the crystallizing pegmatitic magma to cause intense alteration of the enclosing rock was even higher (see Figs 5, 6, 7, 10, and 16).

Relations between the different fluid types

The high-salinity brines (particularly those preserved in the granitic gneiss) must pre-date fluid infiltration. However, under the peak-metamorphic conditions, the possible mixing of brines and the dehydration fluid (homogeneous $H_2O + CO_2$) can be excluded. This is because of the presumed high salinity of the brines in the original migmatized granitic gneiss. The carbonic and brine inclusions are best preserved in the central part of the dehydration zone and, in spite of later modifications, reflect the fluid that controlled the dehydration. The pure CO_2 inclusions could have been derived from the original fluid responsible for the dehydration event, either by unmixing or by water leakage. However, unmixing is considered to be more likely, as this would explain the progressive density decrease related to isothermal uplift. Unmixing more efficiently reduces the CO_2 density in a homogeneous H_2O–CO_2 mixture compared with water leakage. Furthermore, the progressive salinity decrease in the dehydration zone (Figs 14 and 16) can be interpreted as the result of mixing with water, which was separated during unmixing (J. Touret, personal communication, 2005). This process resulted in a water-rich phase of lower salinity and a CO_2-rich phase containing the brine. As late aqueous inclusions generally show a higher T_h compared with the brine inclusions, this suggests that the *PT* path, after the dehydration event, must have followed, in part, a higher geothermal gradient (>50°/km), which is typical for near-isothermal uplift [see (III) in Fig. 17]. Such an uplift path would explain the poor preservation of the original fluid density. This is because differences between fluid and lithostatic pressures would result in decrepitation (i.e. 'explosion' decrepitation or fluid overpressure) in the inclusions, during isothermal decompression. The latest uplift trajectory may have been characterized by 'implosion' decrepitation (i.e. fluid underpressure) of the fluid inclusions resulting in a higher fluid density [see (IV) in Fig. 17].

Furthermore, the pure water introduced after the dehydration event must have disturbed the original fluid contrasts by the local mixing of saline and pure water in the fluid inclusions. This pure water, trapped at upper-crustal levels, is probably of meteoric origin. The scattering of the homogenization and melting temperatures as seen in Fig. 14 can be explained as the combined effect of mixing and fluid inclusion modification.

COMPARISON WITH OTHER LOCALIZED DEHYDRATION ZONES

In addition to the present study, a number of workers (e.g. Kumar & Chacko, 1986; Stähle *et al.*, 1987; Burton & O'Nions, 1990; Raith & Srikantappa, 1993; Todd & Evans, 1994) have published both whole-rock and trace element data comparing a localized orthopyroxene-bearing dehydration zone with the surrounding amphibolite-facies gneiss. For each of these cases, dehydration occurred under *PT* conditions similar to those at Söndrum. A CO_2-rich fluid is held responsible as the dehydration mechanism for most of these examples. The one exception is the study by Burton & O'Nions (1990), which invokes partial melts. Whole-rock data (Table A1) indicate that the dehydration event at Söndrum was principally an isochemical event with trends in element depletion and enrichment seen on a local scale in the mineral chemistry across the traverse (Figs 5–7 and 10). Exceptions include preferential depletion in the HREE, enrichment in Ba and Sr, and depletion in F (Table A1; Figs 3 and 8). Kumar & Chacko (1986) also observed isochemical dehydration of an amphibolite-facies grey gneiss, with no visible increase or decrease in the elements analysed. Todd & Evans (1994) observed isochemical dehydration, with the exception of Y (HREE were not measured), which shows some depletion in the dehydration zone relative to the overlying amphibolite-facies gneiss. In contrast to both these studies and this current study, Stähle *et al.* (1987), Burton & O'Nions (1990) and Raith & Srikantappa (1993) observed distinct differences in the whole-rock and trace element chemistry. For example, at Kabbaldurga, southern India, from whole-rock data, Stähle *et al.* (1987) documented enrichment in K, Rb, Ba, and Si, and depletion in Ca in the feldspars, in addition to general depletion in Fe, Mg, Ti, Zn, V, P, Zr, and the (Y + REE), predominantly (Y + HREE). At Kottavattam, southern India, Raith & Srikantappa (1993) observed enrichment in K, Na, Sr, and Ba, and depletion in Mg, Fe, Ti, V, Zr, and (Y + HREE). Lastly, at Kurunegala, Sri Lanka, Burton & O'Nions (1990) found that depletion in Rb, Pb, U, Sr, Sm, and Nd had occurred, with no changes in the abundance of the major elements. The studies of Stähle *et al.* (1987) and Raith & Srikantappa (1993) would suggest that in addition to CO_2, the dehydrating fluid had a significant KCl–NaCl–$CaCl_2$ brine component, which could account for the variability and mobility

of K, Na, Ca, Sr, Rb, Ba, and the LREE (see previous discussion). At the same time, in an open system, a brine component could also be responsible for the depletion in metal cations such as Fe, Mg, Ti, and Zn as a result of complexing with Cl. With the exception of the Burton & O'Nions (1990) study, what is most intriguing is that, in each example including the present study, Y and the HREE (where tabulated) have lower abundances in the orthopyroxene ± clinopyroxene-bearing dehydrated rock than in the original amphibolite-facies gneiss. As already noted above, Y and the HREE prefer to complex with F as opposed to Cl. This would suggest that a F component was present in each of the dehydrating fluids. Besides an external source, F could also have come from the breakdown of biotite and amphibole during the dehydration event.

LOCALIZED, FLUID-INDUCED, SOLID-STATE DEHYDRATION AT SÖNDRUM

Low H_2O activities ($a_{H_2O} = 0{\cdot}36; X_{H_2O} = 0{\cdot}25$), as defined by orthopyroxene–biotite–K-feldspar–quartz, indicate that the fluids responsible for the dehydration event must have been present before the H_2O-rich melt responsible for the pegmatoid dyke. A CO_2-rich fluid with an H_2O activity of 0·36 could not have caused partial melting of the granitic gneiss at 700°C, either *in situ* or elsewhere. Rather, the fluid responsible must have had an H_2O activity of at least 0·8, which would lie well within the biotite–quartz stability field as opposed to orthopyroxene–K-feldspar (see Fig. 12). In addition, the very low solubility of CO_2 in felsic melts (e.g. Ebadi & Johannes, 1991), coupled with the small volume of granitic melt represented by the pegmatoid dyke, would argue against such a melt being the principal source of CO_2. In the dehydration zone, mineral textures and whole-rock chemistry give no evidence for partial melting nor that the dehydration zone might represent a restite from which H_2O-rich melts could have been extracted. Lastly, the relatively sharp contact between the pegmatoid dyke and the dehydration zone (Fig. 2a) suggests that the granitic melt responsible for it originated elsewhere and was later injected along the tectonic fracture after the actual dehydration event had occurred. *In situ* localized partial melting would have produced a more gradual transition between the pegmatoid dyke and the dehydration zone.

Fluid inclusion data from all three zones suggest that whatever fluids were present during the dehydration event probably consisted of three phases (i.e. CO_2, NaCl, and H_2O), although their exact proportions are not discernible. Experimental data on CO_2–NaCl–H_2O fluids (Johnson, 1991; Gibert *et al.*, 1998; Shmulovich & Graham, 2004) suggest that, at 700°C and 800 MPa, the fluid would consist of two phases, CO_2 and an NaCl brine. The limited extent of the dehydration zone (Holness, 1997; Gibert *et al.*, 1998), coupled with the fluid inclusion data, would imply that CO_2 was the principal component relative to NaCl brines. The presence of an NaCl brine, in fact, could be simply residual, dating from the migmatization of the original granitic gneiss. Evidence that an NaCl-rich brine was probably present during migmatization can be seen in the albitic rims along plagioclase grain boundaries, albitic rim intergrowths into the K-feldspar, the 20% albitic component in the K-feldspar, and the 80% albitic component in the plagioclase, as well as the fact that halogen-bearing minerals in the granitic gneiss tend to be more Cl enriched than the same minerals in the dehydration zone.

The two separate events (i.e. first dehydration of the surrounding granitic gneiss followed by injection of the granitic melts responsible for the pegmatoid dyke) would presumably have produced different effects with respect to the mineral chemistry, whole-rock data, and fluid inclusion data currently documented across the dehydration zone into the granitic gneiss (Figs 3, 5–8, and 10). During formation of the dehydration zone, fluid flow would have been purely advective as the CO_2-rich fluid moved out from the central tectonic fracture into the surrounding granitic gneiss, lowering the H_2O activity, and subsequently causing the partial, solid-state breakdown of biotite and amphibole to orthopyroxene and minor clinopyroxene. At the same time, the released Ca was apparently partitioned back into the amphibole (Fig. 6d). More importantly, the released Ti was partitioned back into the remaining biotite and amphiboles, which acted to stabilize them against further conversion to pyroxenes (Figs 5a and 6a). Fluorine shows some evidence of advective depletion in fluorapatite (Fig. 10c), whereas Cl shows advective depletion in fluorapatite as well as biotite and amphibole (Figs 5e, 6h, and 10d). Both halogens would have been released into the grain boundary fluids, and then apparently partitioned into the mobile fluids present in the tectonic fracture such that they were removed from the locality. The most likely explanation as to why a uniform depletion is seen in (Y + HREE) across the dehydration zone (see Table A1; Figs 3, 8, and 10b) could be complexing with F (see the previous discussion). However, uniform depletion in Cl in all halogen-bearing minerals would suggest that Cl was evidently much more mobile. Yet the fact that the allanite in the dehydration zone appears to be unaltered compared with the allanite in the granitic gneiss, as well as the lack of depletion in LREE in other minerals, despite the affinity of LREE to complex with Cl (see the previous discussion), would imply that (1) there was considerably more F available in the dehydrating fluid than that supplied by the fluorapatite or (2) the affinity of the

(Y + HREE) for F is considerably greater than that of the LREE for Cl, or both (1) and (2).

Later emplacement of the granitic melt responsible for the pegmatoid dyke was the chief vehicle for causing the diffusion of various elements both throughout the dehydration zone as well as in the granitic gneiss. This is seen in the biotite and amphibole mineral chemistry, which indicate that the influence of the granitic melt was felt deep within the granitic gneiss, primarily in its behaviour as a strong chemical sink for F (Figs 5d and 6g). This influence was facilitated probably by NaCl brine-rich fluids along grain boundaries, which presumably were pervasive throughout the dehydration zone as well as regionally throughout the surrounding granitic gneiss. In addition, their presence would have also allowed for the high mobility of Fe and (Y + HREE) along grain boundaries towards the chemical potential sink represented by the granitic melt.

Although not easily discernible, the presence of clinopyroxene zones in the dehydration zone, both at the contact with the pegmatoid dyke as well as at the contact with the granitic gneiss, suggests that mechanical dispersion could have also played a role (see Fetter, 1985). The clinopyroxene zone, at the boundary between the dehydration zone and the pegmatoid dyke, could be the product of higher H_2O activities as a result of the proximity of the granitic melt as well as H_2O expelled by the crystallizing melt during formation of the pegmatoid dyke. In the case of the clinopyroxene zone at the boundary between the dehydration zone and the granitic gneiss, increased H_2O activities could be the result of an H_2O front pushed outward by the CO_2-rich dehydrating fluid, in addition to be mixing at the boundary with the more H_2O-rich fluids from the granitic gneiss. This scenario appears to be supported by the fluid inclusion data (see Fig. 16). The H_2O in such a front would be supplied by the breakdown of biotite and amphibole to pyroxenes. In either zone, formation of only clinopyroxene apparently reflects the H_2O activities present during crystallization of the pegmatoid dyke at presumably 650–700°C ($a_{H_2O} > 0{\cdot}8$; see Fig. 12), where coexisting clinopyroxene and amphibole are also found, and water activities are lower than those in the granitic gneiss, where no clinopyroxene is found. In addition, either zone would appear to reflect higher Ca activities in the fluid as well.

It is interesting to note that the second elongated 'fracture controlled' dehydration zone along the eastern quarry wall, opposite the studied one in the Söndrum quarry, probably represents a continuation of the Söndrum dehydration zone–pegmatoid dyke complex, except that this dehydration zone consists only of a 0·5 m wide clinopyroxene-rich zone with a surrounding 0·5 m wide, diffuse, orthopyroxene- and clinopyroxene-bearing zone overprinting the granitic gneiss. This suggests the separation of two fluids flowing up the tectonic fracture marked by the clinopyroxene-rich zone, with the more CO_2-rich fluid partitioning off to also dehydrate the surrounding granitic gneiss. If this eastern dehydration zone indeed is a continuation of the western Söndrum dehydration zone–pegmatoid dyke complex, it is also an indication of what the western dehydration zone may have looked like before emplacement of the granitic melts responsible for the pegmatoid dyke; that is, a more H_2O-rich clinopyroxene zone surrounded by a relatively more H_2O-poor orthopyroxene-bearing zone. It would also imply that in three dimensions, one possible shape for the pegmatoid dyke–dehydration zone complex at Söndrum could be in the form of an elongated ellipsoid whose centre consists of the pegmatoid dyke surrounded by concentric rings consisting of an inner clinopyroxene zone, an orthopyroxene zone, and an outer clinopyroxene zone.

The source of the fluid responsible for the dehydration zone, and ultimately for the pegmatoid dyke, is unknown. Regionally, there are no known, nearby granite bodies of the same age (*c.* 1400 Ma), which could have served as a fluid source. One possibility could be that the CO_2-rich fluids were forced up along some tectonic fracture, shear zone, or zone of weakness from below. Gravity maps of the Söndrum area suggest the presence of a body, or perhaps bodies, denser than the local granitic gneiss some kilometres below the present-day erosional surface (Graversen, 1998). Presuming that one of these bodies is a mafic intrusion concurrent with emplacement of the pegmatoid dyke, during crystallization it could have served as a source of the fluids. Other than H_2O, the principal component in the fluids given off by mafic magmas during crystallization would be CO_2 as well as brines such as NaCl [see discussion by Newton *et al.* (1998)]. The scenario described above would suggest that this fluid, at first, was primarily CO_2, which allowed for the formation of the dehydration zone, followed by a much more H_2O-rich fluid, perhaps during the later stages of crystallization of the mafic body, which resulted in the granitic melt responsible the pegmatoid dyke. The proposal that the granitic melt acted as a chemical sink for Cl, F, Fe, and (Y + HREE) relative to the surrounding rock would make sense only if it was an open system, acting as a conduit for the migration of fluid or melts away from this locality into the upper crust along the tectonic fracture. Curiously enough, the Varberg–Torpa charnockite–granite complex is also *c.* 1400 Ma (Åhäll *et al.*, 1997; Christoffel *et al.*, 1999). This suggests that there could be some relationship between the formation of this complex and the fluids or melts responsible for the pegmatoid dyke and surrounding dehydration zone at Söndrum, perhaps in the form of some deep-seated regional magmatic event at this time.

In summary, the pegmatoid dyke, the dehydration zone, the clinopyroxene zones, and the surrounding

granitic gneiss at Söndrum record the superposition of two physical processes, namely advective flow and diffusion. Advection, in the form of CO_2-rich fluids, along what was initially a tectonic fracture of some sort, came first and resulted in the formation of the dehydration zone, and is limited to the margins of the dehydration zone. Advection is reflected in the partial conversion of biotite and amphibole to pyroxenes, coupled with the stabilization of the remaining biotite and amphibole through enrichment in Ti (Figs 5c and 6a). It is also reflected in the uniform enrichment, or the uniform depletion, of a particular element in a particular mineral, such as the uniform depletion of Cl in biotite, amphibole and fluorapatite (Figs 5e, 6h, and 10d) or the uniform enrichment of Ca in amphibole (Fig. 6d). In contrast, diffusion came later, with emplacement of the granitic melt responsible for the pegmatoid dyke. It is not limited to the dehydration zone, but extends far into the granitic gneiss, as is seen in the concentration gradient of F in both biotite and amphibole along the traverse (Figs 5d and 6g). Here, the element diffusion profile in either mineral approximates Fick's Second Law. It represents the element concentrations present in the original interconnected grain boundary fluid, now mirrored in the mineral chemistry, with which the fluid is presumed to have been in local equilibrium. Whereas advective flow and diffusion can overlap in a manner independent of each other, as witnessed by the contrasting behaviours of F and Cl in amphibole or biotite, they can also be influenced by each other such that a profile that is primarily advective also shows some influence from diffusion. This is particularly seen in the behaviour of Na and K in amphibole, or the behaviour of Fe, Mg, and Mn in each of the Fe–Mg silicate minerals (Figs 5–7).

Comparison of the results and conclusions of this study with the many previous studies of localized, solid-state dehydration indicate that, no matter what the fluid source, solid-state breakdown of biotite and amphibole to pyroxenes is a function of low H_2O activity fluid infiltration of the rock, the fluids already present along grain boundaries, and, just as importantly, the chemistry of the Fe–Mg silicate minerals present (i.e. Fe/Mg ratio). All three act in unison to determine the balance and direction of the chemical potentials both in the dehydration zone and beyond into the surrounding, non-dehydrated rock. This interaction not only manifests itself in the lowering of H_2O activities beneath a certain threshold so as to allow for pyroxene formation, but also leaves behind additional chemical fingerprints in the metal cation, halogen, and (Y + REE) chemistry of the silicate and phosphate minerals, which are themselves mirrors of both the chemistry of the fluids present during the dehydration event as well as the extent of their total interaction with the rock at large.

ACKNOWLEDGEMENTS

Lund University is thanked for providing funds for field work, whole-rock chemical analyses and PIXE analyses. David Cornell, at the Department of Geology, University of Gothenburg, is thanked for helping with the LA-ICP-MS analyses of the garnets. Jennifer Hein and Sabine Schumann at the GeoForschungsZentrum are thanked for performing the whole-rock F, CO_2, and H_2O analyses. Helga Kemnitz is thanked for assistance with the scanning electron microscope. Dieter Rhede and Oona Appelt are thanked for help with the electron microprobe. Geoff Grantham and Oleg Safanov are thanked for calculating the biotite–quartz–orthopyroxene–K-feldspar H_2O activities used in this study. Ed Hansen and Wilhelm Heinrich are thanked for reading an earlier draft of this manuscript. Bob Newton, Jacques Touret, M. Santosh, and J. Vander Auwera are thanked for their thorough and very thoughtful reviews. Their hard work has made this study a much better paper. Finally, Rolf Romer is thanked for bringing the existence of Söndrum to the first author's attention and then introducing the first author to the second author, which ultimately made this study a reality.

SUPPLEMENTARY DATA

Supplementary data for this paper are available at *Journal of Petrology* online.

REFERENCES

Åhäll, K. I., Samuelsson, L. & Persson, P. O. (1997). Geochronology and structural setting of the 1·38 Ga Torpa granite; implications for charnockite formation in SW Sweden. *Geologiska Föreningens i Stockholm Förhandlingar* **119**, 37–43.

Anders, E. & Grevesse, N. (1989). Abundances of the elements: meteoric and solar. *Geochimica et Cosmochimica Acta* **53**, 197–214.

Andersen, T., Whitehouse, M. J. & Burke, E. A. J. (1997). Fluid inclusions in Scourian granulites from the Lewisian complex of NW Scotland: evidence for CO_2-rich fluid in late Archean high-grade metamorphism. *Lithos* **40**, 93–104.

Andersson, J., Söderlund, U., Cornell, D., Johansson, L. & Möller, C. (1999). Sveconorwegian (-Grenvillian) deformation, metamorphism and leucosome formation in SW Sweden, SW Baltic Shield; constraints from a Mesoproterozoic granite intrusion. *Precambrian Research* **98**, 151–171.

Aranovich, L. Y. & Berman, R. G. (1997). A new garnet–orthopyroxene thermometer based on reversed Al_2O_3 solubility in $FeO–Al_2O_3–SiO_2$ orthopyroxene. *American Mineralogist* **82**, 345–353.

Bakker, R. J. (2003). Package FLUIDS 1. Computer programs for analysis of fluid inclusion data and for modelling bulk fluid properties. *Chemical Geology* **194**, 3–23.

Berman, R. G. (1988). Internally-consistent thermodynamic data for minerals in the system $Na_2O–K_2O–CaO–MgO–FeO–Fe_2O_3–Al_2O_3–SiO_2–TiO_2–H_2O–CO_2$. *Journal of Petrology* **29**, 445–522.

Berman, R. G. (1990). Mixing properties of Ca–Mg–Fe–Mn garnets. *American Mineralogist* **75**, 328–344.

Berman, R. G., Aranovich, L. Ya. & Pattison, D. R. M. (1995). Reassessment of the garnet–clinopyroxene Fe–Mg exchange thermometer: II. Thermodynamic analysis. *Contributions to Mineralogy and Petrology* **119**, 30–42.

Bi, X., Cornell, D. H. & Hu, R. (2001). REE composition of primary and altered feldspar from the mineralized alteration zone of alkaline intrusive rocks, Western Yunnan Province, China. *Ore Geology Reviews* **19**, 69–78.

Brenan, J. M. & Watson, E. B. (1988). Fluids in the lithosphere, 2. Experimental constraints on CO_2 transport in dunite and quartzite at elevated *P–T* conditions with implications for mantle and crustal decarbonation processes. *Earth and Planetary Science Letters* **91**, 141–158.

Burton, K. W. & O'Nions, R. K. (1990). The timescale and mechanism of granulite formation at Kurunegala, Sri Lanka. *Contributions to Mineralogy and Petrology* **106**, 66–89.

Carignan, J., Hild, P., Mevelle, G., Morel, J. & Yeghicheyan, D. (2001). Routine analysis for major and trace element concentrations of geological samples using ICP-AES and ICP-MS. In: *Abstracts, Geoanalysis 2000, 4th International Conference on the Analysis of Geological and Environmental Materials, 30 August–1 September, 2000, Abbaye des Prémontrés, France*, p. 144.

Christoffel, C. A., Connelly, J. N. & Åhäll, K.-I. (1999). Timing and characterization of recurrent pre-Sveconorwegian metamorphism and deformation in the Varberg–Halmstad region of SW Sweden. *Precambrian Research* **98**, 173–195.

Connelly, J. N., Berglund, J. & Larson, S. A. (1996). Thermotectonic evolution of the Eastern Segment of southwestern Sweden: tectonic constraints from U–Pb geochronology. In: Brewer, T. S. (ed.) *Precambrian Crustal Evolution in the North Atlantic Region. Geological Society, London, Special Publications* **112**, 297–313.

Dobmeier, C. & Raith, M. M. (2000). On the origin of 'arrested' charnockitization in the Chilka Lake area, Eastern Ghats Belt, India: a reappraisal. *Geological Magazine* **137**, 27–37.

Ebadi, A. & Johannes, W. (1991). Beginning of melting and composition of first melts in the system Qz–Ab–Or–H_2O–CO_2. *Contributions to Mineralogy and Petrology* **106**, 286–295.

Ernst, W. G. & Liu, J. (1998). Experimental phase-equilibrium study of Al- and Ti-contents of calcic amphibole in MORB—a semiquantitative thermobarometer. *American Mineralogist* **83**, 952–969.

Fetter, C. W. (1985). *Contaminant Hydrogeology*. New York: Macmillan, 554 pp.

Fonarev, V. I., Santosh, M., Vasiukova, O. V. & Filimonov, M. B. (2003). Fluid evolution and exhumation path of the Trivandrum granulite block, southern India. *Contributions to Mineralogy and Petrology* **145**, 339–354.

Förster, H.-J., Tischendorf, G., Trumbull, R. B. & Gottesmann, B. (1999). Late-collisional granites in the Variscan Erzgebirge, Germany. *Journal of Petrology* **40**, 1613–1645.

Friend, C. R. L. (1981). Charnockite and granite formation and influx of CO_2 at Kabbaldurga. *Nature* **294**, 550–552.

Frost, B. R. (1991). Introduction to oxygen fugacity and its petrologic importance. In: Lindsley, D. H. (ed.) *Oxide Minerals*: *Petrologic and Magnetic Significance. Mineralogical Society of America, Reviews in Mineralogy* **25**, 1–9.

Fuhrman, M. L. & Lindsley, D. H. (1988). Ternary feldspar modelling and thermometry. *American Mineralogist* **73**, 201–215.

Ghiorso, M. S. & Sack, R. O. (1991). Fe–Ti oxide geothermometry: thermodynamic formulation and the estimation of intensive variables in silicic magmas. *Contributions to Mineralogy and Petrology* **108**, 485–510.

Gibert, F., Guillaume, D. & Laporte, D. (1998). Importance of fluid immiscibility in the H_2O–NaCl–CO_2 system and selective CO_2 entrapment in granulites: experimental phase diagram at 5–7 kbar, 900°C and wetting textures. *European Journal of Mineralogy* **10**, 1109–1123.

Govindaraju, K. (1994). 1994 compilation of working values and sample description for 383 geostandards. *Geostandards Newsletter* **18**, 1–158.

Graham, C. M. & Powell, R. (1984). A garnet–hornblende geothermometer: calibration, testing, and application to the Pelona Schist, Southern California. *Journal of Metamorphic Geology* **2**, 13–31.

Graversen, O. (1998). Mantle diapir below the Fennoscandian border zone. *23rd Nordic Geological Winter Meeting, Århus*, p. 90.

Haas, J. R., Shock, E. L. & Sasani, D. C. (1995). Rare earth elements in hydrothermal systems: estimates of standard partial molal thermodynamic properties of aqueous complexes of the rare earth elements at high pressures and temperatures. *Geochimica et Cosmochimica Acta* **59**, 4329–4350.

Hansen, E. C., Newton, R. C. & Janardhan, A. S. (1984). Fluid inclusions in rocks from the amphibolite-facies gneiss to charnockite progression in southern Karnataka, India: direct evidence concerning the fluids of granulite metamorphism. *Journal of Metamorphic Geology* **2**, 249–264.

Hansen, E. C., Janardhan, A. S., Newton, R. C., Prame, W. K. B. N. & Kumar, G. R. R. (1987). Arrested charnockite formation in southern India and Sri Lanka. *Contributions to Mineralogy and Petrology* **96**, 225–244.

Hansen, E. C., Khurram, A. & Harlov, D. E. (2002). Rb depletion in biotites and whole rocks across an amphibolite to granulite-facies transition zone, Tamil Nadu, south India. *Lithos* **64**, 29–47.

Harley, S. L. & Santosh, M. (1995). Wollastonite at Nuliyam, Kerala: a reassessment of CO_2 infiltration and charnockite formation at a classic locality. *Contributions to Mineralogy and Petrology* **20**, 83–94.

Harlov, D. E. (1992). Comparative oxygen barometry in granulites, Bamble Sector, SE Norway. *Journal of Geology* **100**, 447–464.

Harlov, D. E. (2000*a*). Pressure–temperature estimation in orthopyroxene–garnet bearing granulite-facies rocks, Bamble Sector, Norway. *Mineralogy and Petrology* **69**, 11–33.

Harlov, D. E. (2000*b*). Titaniferous magnetite–ilmenite thermometry/titaniferous magnetite–ilmenite–orthopyroxene–quartz oxygen barometry in orthopyroxene-bearing granulite-facies gneisses, Bamble Sector, SE Norway: implications for the role of high grade CO_2-rich fluids during granulite genesis. *Contributions to Mineralogy and Petrology* **139**, 180–197.

Harlov, D. E. & Förster, H.-J. (2002*a*). High-grade fluid metasomatism on both a local and regional scale: the Seward Peninsula, Alaska and the Val Strona di Omegna, Ivrea–Verbano Zone, northern Italy. Part I: Petrography and silicate mineral chemistry. *Journal of Petrology* **43**, 769–799.

Harlov, D. E. & Förster, H.-J. (2002*b*). High-grade fluid metasomatism on both a local and regional scale: the Seward Peninsula, Alaska and the Val Strona di Omegna, Ivrea–Verbano Zone, northern Italy. Part II: Phosphate mineral chemistry. *Journal of Petrology* **43**, 801–824.

Harlov, D. E. & Förster, H.-J. (2003). Fluid-induced nucleation of REE-phosphate minerals in apatite: nature and experiment. Part II. Fluorapatite. *American Mineralogist* **87**, 245–261.

Harlov, D. E.,Newton, R. C., Hansen, E. C. & Janardhan, A. S. (1997). Oxide and sulfide minerals in highly oxidized, Rb-depleted, Archean granulites of the Shevaroy Hills Massif, South India: oxidation states and the role of metamorphic fluids. *Journal of Metamorphic Geology* **15**, 701–717.

Harris, N. B. W. & Bickle, M. J. (1989). Advective fluid transport during charnockite formation: an example from southern India. *Earth and Planetary Science Letters* **93**, 151–156.

Harris, N. B. W., Jackson, D. H., Mattey, D. P., Santosh, M. & Bartlett, J. (1993). Carbon-isotope constraints on fluid advection during contrasting examples of incipient charnockite formation. *Journal of Metamorphic Geology* **11**, 833–843.

Henry, D. J., Guidotti, C. V. & Thomson, J. A. (2005). The Ti-saturation surface for low-to-medium pressure metapelitic biotites: implications for geothermometry and Ti-substitution mechanisms. *American Mineralogist* **90**, 316–328.

Holdaway, M. J., Mukhopadhyay, B., Dyar, M. D., Guidotti, C. V. & Dutrow, B. L. (1997). Garnet–biotite geothermometry revised: new Margules parameters and a natural specimen data set from Maine. *American Mineralogist* **82**, 582–595.

Holland, T. J. B. & Powell, R. (1998). An internally consistent thermodynamic data set for phases of petrological interest. *Journal of Metamorphic Geology* **16**, 309–343.

Holness, M. B. (1997). Surface chemical controls on pore-fluid connectivity in texturally equilibrated materials. In: Jamtveit, B. & Yardley, B. W. D. (eds) *Fluid Flow and Transport in Rocks*. London: Chapman & Hall, pp. 149–169.

Jackson, D. H. & Santosh, M. (1992). Dehydration reaction and isotope front transport induced by CO_2 infiltration in Nuliyam, South India. *Journal of Metamorphic Geology* **10**, 365–382.

Jarosewich, E. & Boatner, L. A. (1991). Rare-earth element reference samples for electron microprobe analysis. *Geostandards Newsletter* **15**, 397–399.

Jarosewich, E., Nelen, J. A. & Norberg, J. A. (1980). Reference samples for electron microprobe analysis. *Geostandards Newsletter* **4**, 43–47.

Johansson, A., Meier, M., Oberli, F. & Wikman, H. (1993). The early evolution of the Southwest Swedish Gneiss Province: geochronological and isotopic evidence from southernmost Sweden. *Precambrian Research* **64**, 361–388.

Johansson, L. (1998). Charnockitization and polyphase metamorphism in the eastern segment of the southwest Swedish gneiss province. *23rd Nordic Geological Winter Meeting, Århus*, p. 142.

Johansson, L., Möller, C. & Söderlund, U. (2001). Geochronology of eclogite-facies metamorphism in the Sveconorwegian Province of SW Sweden. *Precambrian Research* **106**, 261–275.

Johansson, S. A. E. & Campbell, J. L. (1988). *PIXE: a Novel Technique for Elemental Analysis*. Chichester: John Wiley, 347 pp.

Johnson, E. L. (1991). Experimentally determined limits for H_2O–CO_2–NaCl immiscibility in granulites. *Geology* **19**, 925–928.

Knudsen, T. L. & Lidwin, A. (1996). Magmatic CO_2, brine and nitrogen inclusions in Sveconorwegian enderbitic dehydration veins and a gabbro from the Bamble sector, Southern Norway. *European Journal of Mineralogy* **8**, 1041–1063.

Krüger, Y. & Diamond, L. (2001). *P–V–T–X* properties of two H_2O–CO_2–NaCl mixtures up to 850°C and 500 MPa: synthetic fluid inclusion study. In: Noronha, F., D'pria, A. & Guedes, A. (eds) *XVI ECROFI, Porto, 2001, Abstracts. Faculdade de Ciências do Porto, Departamento de Geologia, Memória* **7**, 241–244.

Kumar, G. R. R. (2004). Mechanism of arrested charnockite formation at Nemmara, Palghat region, southern India. *Lithos* **75**, 331–358.

Kumar, G. R. R. & Chacko, T. (1986). Mechanisms of charnockite formation and breakdown in southern Kerala: implications for the origin of the southern Indian granulite terrain. *Journal of the Geological Society of India* **28**, 277–288.

Larson, S. Å., Berglund, J., Stigh, J. & Tullborg, E.-L. (1990). The Protogine Zone, southwest Sweden: a new model—an old issue. In: Gower, C. F., Rivers, T. & Ryan, A. B. (eds) *Mid-Proterozoic Laurentia–Baltica. Geological Association of Canada, Special Paper* **38**, 317–333.

Larsson, W. (1956). Mapsheet Laholm. Swedish Geological Survey Series Aa 197.

Leake, B. E., Woolley, A. R., Arps, C. E. S., *et al.* (1997). Nomenclature of amphiboles: report of the subcommittee on amphiboles of the international mineralogical association commission on new minerals and mineral names. *Canadian Mineralogist* **35**, 219–246.

Lee, H. Y. & Ganguly, J. (1988). Equilibrium compositions of coexisting garnet and orthopyroxene: experimental determinations in the system FeO–MgO–Al_2O_3–SiO_2, and applications. *Journal of Petrology* **29**, 93–113.

Markl, G. & Piazolo, S. (1998). Halogen-bearing minerals in syenites and high-grade marbles of Dronning Maud Land, Antarctica: monitors of fluid compositional changes during late-magmatic fluid–rock interaction processes. *Contributions to Mineralogy and Petrology* **132**, 246–268.

McGregor, V. R. & Friend, C. R. L. (1992). Late Archean prograde amphibolite- to granulite-facies relations in the Fiskenæsset region, southern west Greenland. *Journal of Geology* **100**, 207–219.

McLelland, J. M., Hunt, W. M. & Hansen, E. C. (1988). The relationships between metamorphic charnockite and marble near Speculator, Central Adirondack Mountains, New York. *Journal of Geology* **96**, 455–468.

Möller, C. (1998). Decompressed eclogites in the Sveconorwegian (Grenvillian) orogen of SW Sweden: petrology and tectonic implications. *Journal of Metamorphic Geology* **16**, 641–656.

Morishita, T., Arai, S. & Green, D. H. (2003). Evolution of low-Al orthopyroxene in the Horoman peridotite, Japan: an unusual indicator of metasomatizing fluids. *Journal of Petrology* **44**, 1237–1246.

Munoz, J. L. (1992). Calculation of HF and HCl fugacities from biotite compositions: revised equations. *Geological Society of America, Abstracts with Programs* **26**, 221.

Newton, R. C. (1983). Geobarometry of high grade metamorphic rocks. *American Journal of Science* **283-A**, 1–28.

Newton, R. C., Aranovich, L. Ya., Hansen, E. C. & Vandenheuvel, B. A. (1998). Hypersaline fluids in Precambrian deep-crustal metamorphism. *Precambrian Research* **91**, 41–63.

Nijland, T. G., Touret, J. L. R. & Visser, D. (1998). Anomalously low temperature orthopyroxene, spinel, and sapphirine occurrences in metasediments from the Bamble amphibolite-to-granulite-facies transition zone (south Norway): possible evidence for localized action of saline fluids. *Journal of Geology* **106**, 575–590.

Page, L. M., Möller, C. & Johansson, L. (1996). ^{40}Ar /^{39}Ar geochronology across the Mylonite Zone and the Southwestern Granulite Province in the Sveconorwegian Orogen of S Sweden. *Precambrian Research* **79**, 239–259.

Pan, Y. & Fleet, M. E. (1996). Rare earth element mobility during prograde granulite-facies metamorphism: significance of fluorine. *Contributions to Mineralogy and Petrology* **123**, 251–262.

Patiño-Douce, A. E. (1993). Titanium substitution in biotite: an empirical model with applications to thermometry, O_2 and H_2O barometries, and consequences for biotite stability. *Chemical Geology* **108**, 133–162.

Pattison, D. R. M., Chacko, T., Farquhar, J. & McFarlane, C. R. M. (2003). Temperatures of granulite-facies metamorphism: constraints from experimental phase equilibria and thermobarometry corrected for retrograde exchange. *Journal of Petrology* **44**, 867–900.

Perchuk, L. L., Safonov, O. G., Gerya, T. V., Fu, B. & Harlov, D. E. (2000). Mobility of components in metasomatic transformation and partial melting of gneisses: an example from Sri Lanka. *Contributions to Mineralogy and Petrology* **140**, 212–232.

Pouchou, J. L. & Pichoir, F. (1985). 'PAP' (φ–ρ–Z) procedure for improved quantitative microanalysis. In: Armstrong, J. T. (ed.) *Microbeam Analysis*. San Francisco, CA: San Francisco Press, pp. 104–106.

Powell, R., Holland, T. & Worley, B. (1998). Calculating phase diagrams involving solid solutions via non-linear equations, with examples using THERMOCALC. *Journal of Metamorphic Geology* **16**, 577–588.

Pownceby, M. I., Wall, V. J. & O'Neill, H. St. C. (1991). An experimental study of the effect of Ca upon garnet–ilmenite Fe–Mn exchange equilibria. *American Mineralogist* **76**, 1580–1588.

Radhika, U. P. & Santosh, M. (1996). Shear-zone hosted graphite in southern Kerala, India: implications for CO_2 infiltration. *Journal of Southeast Asian Earth Sciences* **14**, 265–273.

Raith, M. & Srikantappa, C. (1993). Arrested charnockite formation at Kottavattam, southern India. *Journal of Metamorphic Geology* **11**, 815–832.

Rajesh, H. M., Santosh, M. & Yoshida, M. (1997). Dextral Pan-African shear along the southwestern edge of the Achankovil shear belt, south India: constraints on Gondwana reconstruction—a discussion. *Journal of Geology* **106**, 105–109.

Rimsa, A., Whitehouse, M. J. & Johansson, L. (2003). Behaviour of REE in zircon during charnockitization—a case study from Söndrum, Sweden. *Geophysical Research Abstracts* **5**, 097838.

Sack, R. O. & Ghiorso, M. S. (1989). Importance of considerations of mixing properties in establishing an internally consistent thermodynamic data base: thermochemistry of minerals in the system Mg_2SiO_4–Fe_2SiO_4–SiO_2. *Contributions to Mineralogy and Petrology* **102**, 41–68.

Sack, R. O. & Ghiorso, M. S. (1991*a*). An internally consistent model for the thermodynamic properties of Fe–Mg–titanomagnetite–aluminate spinels. *Contributions to Mineralogy and Petrology* **106**, 474–505.

Sack, R. O. & Ghiorso, M. S. (1991*b*). Chromian spinels as petrogenetic indicators: thermodynamics and a petrologic application. *American Mineralogist* **76**, 827–847.

Santosh, M. (1986). Carbonic metamorphism of charnockites in the southwestern Indian shield: a fluid inclusion study. *Lithos* **19**, 1–10.

Santosh, M. (1992). Carbonic fluids in granulites: cause or consequence? *Journal of the Geological Society of India* **39**, 375–399.

Santosh, M. (2003). Granulites and fluids: a petrologic paradigm. *Geological Society of India Memoir* **52**, 289–311.

Santosh, M. & Radhika, U. P. (1994). Carbonic metasomatism and charnockitic alteration. *Journal of the Geological Society of India* **43**, 191–199.

Santosh, M. & Tsunogae, T. (2003). Extremely high density pure CO_2 fluid inclusions in a garnet granulite from southern India. *Journal of Geology* **111**, 1–16.

Santosh, M. & Wada, H. (1993*a*). Microscale isotopic zonation in graphite crystals: implications for channelised CO_2 influx in granulites. *Earth and Planetary Science Letters* **119**, 19–26.

Santosh, M. & Wada, H. (1993*b*). A carbon isotope study of graphites from Kerala Khondalite Belt, southern India: evidence for CO_2 infiltration in granulites. *Journal of Geology* **101**, 643–651.

Santosh, M., Harris, N. B. W., Jackson, D. H. & Mattey, D. P. (1990). Dehydration and incipient charnockite formation: a phase equilibria and fluid inclusion study from south India. *Journal of Geology* **98**, 915–926.

Santosh, M., Jackson, D. H., Harris, N. B. W. & Mattey, D. P. (1991*a*). Carbonic fluid inclusions in south Indian granulites: evidence for entrapment during charnockite formation. *Contributions to Mineralogy and Petrology* **108**, 318–330.

Santosh, M., Jayananda, M. & Mahabaleswar, B. (1991*b*). Fluid evolution in the Closepet granite: a magmatic source for charnockite formation at Kabbaldurga? *Journal of the Geological Society of India* **38**, 55–65.

Sarkar, S., Santosh, M., Dasgupta, S. & Fukuoka, M. (2003). Very high density CO_2 associated with ultrahigh temperature metamorphism in the Eastern Ghats granulite belt, India. *Geology* **31**, 51–54.

Satish-Kumar, M. & Santosh, M. (1998). A petrological and fluid inclusion study of calc-silicate–charnockite associations from southern Kerala, India: implications for CO_2 influx. *Geological Magazine* **135**, 27–45.

Shepherd, T. J. (1981). Temperature-programmable heating–freezing stage for microthermometric analysis of fluid inclusions. *Economic Geology* **76**, 1244–1247.

Shmulovich, K. I. & Graham, C. M. (2004). An experimental study of phase equilibria in the systems H_2O–CO_2–$CaCl_2$ and H_2O–CO_2–NaCl at high pressures and temperatures (500–800°C, 0·5–0·9 GPa): geological and geophysical applications. *Contributions to Mineralogy and Petrology* **146**, 450–462.

Söderlund, U., Jarl, L. G., Persson, P. O., Stephens, M. B. & Wahlgren, C. H. (1999). Protolith ages and timing of deformation in the eastern, marginal part of the Sveconorwegian orogen, southwestern Sweden. *Precambrian Research* **94**, 29–48.

Söderlund, U., Möller, C., Andersson, J., Johansson, L. & Whitehouse, M. (2002). Zircon geochronology in polymetamorphic gneisses in the Sveconorwegian orogen, SW Sweden: ion microprobe evidence for 1·46-1·42 and 0·98-0·96 Ga reworking. *Precambrian Research* **113**, 193–225.

Srikantappa, C., Raith, M. & Speiring, M. (1985). Progressive charnockitization of a leptynite–khondalite suite in southern Kerala, India—evidence for formation of charnockites through decrease in fluid pressure? *Journal of the Geological Society of India* **26**, 849–872.

Stähle, H. J., Raith, M., Hoernes, S. & Delfs, A. (1987). Element mobility during incipient granulite formation at Kabbaldurga, southern India. *Journal of Petrology* **28**, 803–834.

Todd, C. S. & Evans, B. W. (1994). Properties of CO_2-induced dehydration of amphibole. *Journal of Petrology* **35**, 1213–1239.

Tsunogae, T., Santosh, M., Osanai, Y., Owada, M., Toyoshima, T. & Hokada, T. (2002). Very high-density carbonic fluid inclusions in sapphirine-bearing granulites from Tonagh Island in the Archean Napier Complex, East Antarctica: implications for CO_2 infiltration during ultrahigh (T >1100°C) metamorphism. *Contributions to Mineralogy and Petrology* **143**, 279–299.

van den Kerkhof, A. M. & Grantham, G. H. (1999). Metamorphic charnockite in contact aureoles around intrusive enderbite from Natal, South Africa. *Contributions to Mineralogy and Petrology* **137**, 115–132.

Vander Auwera, J. (1993). Diffusion controlled growth of pyroxene-bearing margins on amphibolite bands in the granulite-facies of Rogaland (Southwestern Norway): implications for granulite formation. *Contributions to Mineralogy and Petrology* **114**, 203–220.

van Reenen, D. D., Roering, C., Smit, C. A., van Schalkwyk, J. F. & Barton, J. M. (1988). Evolution of the northern high-grade margin of the Kaapvaal craton, South Africa. *Journal of Geology* **96**, 549–560.

Wang, X.-D. & Lindh, A. (1996). Temperature–pressure investigation of the southern part of the Southwest Swedish Granulite Region. *European Journal of Mineralogy* **8**, 51–67.

Wang, X. D., Page, L. M. & Lindh, A. (1996). $^{40}Ar/^{39}Ar$ geochronological constraints from the southeasternmost part of the eastern segment of the Sveconorwegian orogeny: implications for timing of granulite-facies metamorphism. *Geologiska Föreningens i Stockholm Förhandlingar* **118**, 1–8.

Watson, E. B. & Brenan, J. M. (1987). Fluids in the lithosphere, 1. Experimentally determined wetting characteristics of CO_2–H_2O fluids and their implications for fluid transport, host-rock physical

properties, and fluid inclusion formation. *Earth and Planetary Science Letters* **85**, 594–615.

Yoshida, M. & Santosh, M. (1994). A tectonic perspective of incipient charnockite formation in East Gondwana. *Precambrian Research* **66**, 379–392.

Yoshida, M., Santosh, M. & Shirahata, H. (1991). Geochemistry of gneiss–granulite transformation in the 'incipient charnockite' zones of southern India. *Mineralogy and Petrology* **45**, 69–83.

Zhu, C. & Sverjensky, D. A. (1991). Partitioning of F–Cl–OH between minerals and hydrothermal fluids. *Geochimica et Cosmochimica Acta* **55**, 1837–1858.

Zhu, C. & Sverjensky, D. A. (1992). F–Cl–OH partitioning between biotite and apatite. *Geochimica et Cosmochimica Acta* **56**, 3435–3467.